Large Eddy Simulations of mean pressure and H_2 addition effects on the stabilization and dynamics of a partially-premixed swirled-stabilized methane flame

P. W. Agostinelli[a,b,*], D. Laera[b], I. Chterev[c], I. Boxx[c], L. Gicquel[b], T. Poinsot[d]

[a]*Safran Helicopter Engines, 64510 Bordes, France*
[b]*CERFACS, 42 avenue Gaspard Coriolis, 31057 Toulouse, France*
[c]*Institut für Verbrennungstechnik, Deutsches Zentrum für Luft-und Raumfahrt (DLR), Stuttgart, Germany*
[d]*Institut de Mécanique des Fluides de Toulouse, IMFT, Université de Toulouse, CNRS, Toulouse 31400, France*

Abstract

This work analyses pressure and hydrogen enrichment effects on the stabilization and combustion dynamics of a partially-premixed swirled-stabilized methane flame operated at 1, 3 and 5 bar, with H_2 admixture up to 40% by volume. Large Eddy Simulation (LES) is performed to analyze flame stabilization and dynamics for all cases. Since both turbulence and chemical time scales are significantly affected by pressure, it is a challenge for LES to compute such changes. The thickened flame (TFLES) model is used here with a Static Mesh Refinement (SMR) strategy to describe flame turbulence interactions to ensure that all flames are resolved similarly at 1, 3 and 5 bar. This necessitates a significant increase in the required mesh size. An Analytically Reduced Chemistry (ARC) scheme is employed to describe CH_4-H_2/Air chemistry. LES is validated against experimental multi-kHz repetition-rate

*Corresponding author: agostinelli@cerfacs.fr

OH* chemiluminescence, OH Planar Laser Induced Fluorescence (PLIF), stereoscopic Particle Image Velocimetry (sPIV) and pressure recordings, with all predictions providing satisfactory agreement. The dynamics of the different flames are then addressed. First, the impact of hydrogen at atmospheric pressure is investigated. While the reference natural gas flame (1 bar, 0% H_2) presents a lifted M-shape with a strong Precessing Vortex Core (PVC), 40% H_2-enrichment modifies the flame which becomes an attached V-shape, with a weakened PVC and the triggering of a thermoacoustic oscillation at the system first acoustic mode. Second, the impact of mean pressure is analyzed by fixing the H_2-enrichment while increasing the mean pressure to 3 and then 5 bar. As the pressure increases, the flame becomes more compact and the chemical as well as the turbulent time scales change, potentially affecting the flame/turbulence interaction. For these points, the thermoacoustic oscillation at the first system acoustic mode rapidly disappears and stable conditions are recovered.
Keywords: Elevated pressure, H_2-enrichment, Thermoacoustic instabilities, Large Eddy Simulation, Turbulent flames, Hydrodynamic instabilities

---

1. Introduction

As society evolves towards a green economy to face the global climate change, the combustion community is expected to develop new technologies and design low emission combustors for the aviation and energy sectors. Such design however still remains a challenge because lean combustion systems, which is the path for low pollutant emissions, are more prone to different flame dynamics issues, such as thermoacoustic instabilities [1, 2], lean blow-off [3, 4] and extinctions [5]. In the past decades, Large Eddy Simulation (LES) have been widely used to support this research process demonstrating its large potential in predicting reactive flows in complex industrial geometries [1, 6, 7]. Nevertheless, the majority of studies have been performed in academic test rigs where power density and pressure are usually scaled down. Therefore, a complete understanding of the impact of elevated pressure on the flame shape and its dynamics is needed for real engines applications [8].

High fidelity measurements comprising high-speed Particle Image Velocimetry (PIV) and OH Planar Laser Induced Fluorescence (OH-PLIF) on both gas turbine [9–11] and aero-engines pressurised systems [12, 13] have been proposed at DLR test facilities. Similar studies have been performed by other research groups, for example at Purdue University [14], Coria laboratory [15] and Georgia Tech University [16]. In all these studies on different configurations, a more compact flame structure was obtained as pressure increased. When it comes to combustion instabilities, it has been shown that pressure can change the flame oscillation amplitude and phase [17] as well as the interaction between the flame and the vortices, potentially affecting the flame response to acoustic perturbation [18–20]. Furthermore, hydro-

dynamic instabilities, such as Helical Vortices (HV) in the shear layers and a Precessing Vortex Core (PVC) in the Central Recirculation Zone (CRZ), coupled with thermoacoustic oscillations have been observed even at elevated pressure despite very different hydrodynamic time-scales if compared to the equivalent atmospheric configuration [21, 22].

LES has been widely applied to turbulent reacting flows in real gas-turbine combustors at elevated power density, focusing on flame stabilization, dynamics and even pollutant emissions [6]. Moin *et al.* [23] and Boudier *et al.* [24, 25] assessed the predictive capability of a low-Mach-number and a compressible LES code, respectively, on a combustor operated at high pressure, achieving good agreement with experimental data. Schmitt *et al.* [26] analyzed the combustion instability in a realistic gas turbine combustion chamber while identifying also the mechanism at the base of the thermoacoustic oscillation performing a first prediction of the nitric oxide emissions levels. Jaravel *et al.* [27] used high-fidelity LES coupled with an Analytically Reduced Chemistry (ARC) to predict pollutant formation in a real engine configuration, showing that mixing and strain are playing a significant role. More recently, Legros *et al.* [28] conducted an experimental and numerical study of a lean premixed liquid injection system designed for helicopter engines with a pressure ranging from 4 to 18 bar, focusing on the impact of the fuel droplet distribution on the flame structure.

The addition of hydrogen (or hydrogen-rich gases) in existing gas turbines as a solution to decarbonize aviation and energy sectors is a second challenge [29–32]. When mixed to classical hydrocarbon fuels, hydrogen increases the mixture laminar flame speed [33–35], while extending the lean

blow-off and extinction limits [36, 37]. A direct consequence of these observations is that hydrogen modifies the flame shape [38, 39] and the heat release rate distribution in more complex swirled-stabilized flames [40–43]. H_2-addition have also an impact on flame dynamics [44]. Hydrodynamic instabilities, such as PVC and HV, have been reported as sensitive to hydrogen enrichment [45] since they are susceptible to the density field non-homogeneities [46, 47]. Recently, Beita *et al.* [48] presented a review of the hydrogen enrichment impact on combustion instabilities for gas turbine applications. Hydrogen can affect the gain and phase of the Flame Transfer Function (FTF) [49, 50] changing thermoacoustic coupling and system stabilization [51–55]. Very recently, the PRECCINSTA combustor has been fueled with different H_2-enrichment levels to study the impact on the flame stabilization and dynamics at atmospheric pressure [56, 57].

Few experimental works have focused on the effect of hydrogen addition in combustors operated at elevated pressure. Zhang *et al.* [42] operated a low swirl burner with different bulk velocities, hydrogen enrichment, equivalence ratios and pressures up to 3 bar. Experiments showed that hydrogen can trigger thermoacoustic instabilities. In parallel, the HIPOT PRECCINSTA burner was operated by Chterev and Boxx [45] at elevated pressure (up to 5 bar) with different hydrogen enrichment levels, presenting the impact on the flame shape, PVC and thermoacoustic frequency as well as its amplitude. H_2 enrichment in that case increases the phase delay between the oscillating pressure field and the heat release by decreasing the flame length while simultaneously increasing the sound speed in the combustor. Indlekofer *et al.* [58] operated an annular combustion chamber at intermediate pressures

(up to 3.3 bar) with CH_4-H_2 blends for which different azimuthal thermoacoustic instabilities appeared. Here again pressure is shown to mainly affect the flame height and intensity during the high-amplitude instabilities, while only marginally affecting the low-amplitude ones. The same rig was subsequently operated by Ahn *et al.* [59] to investigate the effect of equivalence ratio variation on the flame transient thermoacoustic response.

To the best of the authors' knowledge, there is still no specific numerical work investigating the effects of both pressure and hydrogen enrichment on the flame stabilization and its dynamics. This work aims at filling this gap by performing LES of the PRECCINSTA HIPOT burner enriched with hydrogen (up to 40% by vol.) and operated at elevated pressure (up to 5 bar). Sections 2 and 3 describe the experimental and numerical setup, respectively, underlining the modeling challenges of predicting high power density flows. The impact of hydrogen enrichment at atmospheric pressure is discussed in section 4. Finally, the effect of elevated pressure while keeping the same H_2-enrichment level is investigated in section 5. As pressure increases, flames get more compact, the thermoacoustic oscillation disappears and the chemical as well as the turbulent time scales significantly change affecting the flame/turbulence interaction.

2. Experimental setup

In this study, the well-known PRECCINSTA gas turbine model combustor was modified for use at elevated pressure conditions and operated in the High-Pressure Optical Testrig (HIPOT) ad DLR. The burner and test rig are shown in Fig. 1 [21, 22, 45]. In this setup, dry pre-heated air is fed through

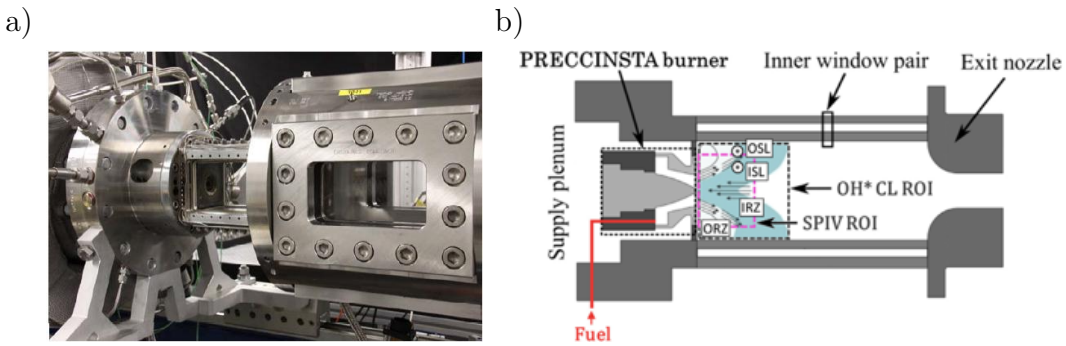

Figure 1: (a) Picture and (b) schematic of the experimental test bench showing the injector with the combustion chamber. Region of Interest for experimental diagnostics is also indicated [45].

the plenum and 12 radial swirl channels impose a swirling motion to the flow before entering the combustion chamber. Hydrogen-enriched natural gas[1] is injected into the air stream through 12 small holes of 1 mm in diameter located within the radial swirler in a "technically premixed" mode. The combustion chamber has a square section of 80 x 80 mm^2, a total length of 200 mm and quartz windows to allow optical access for diagnostics. The combustion chamber windows are double-paned, with a stream of cooling air forced between them in a technique known as "back-face cooling". This ensures window survivability at thermal load conditions without directly affecting the fluid-dynamics of the combustion. Its effect on heat-transfer at the wall, however, must be considered in high fidelity numerical simulations of this configuration. The burner itself is also cooled using a stream of cooling air forced through internal channels below the backplane. Hot gases exit the

[1]Natural gas composition was 93% CH_4, 4% C_2H_6, 1.5% N_2, 1% CO_2, and 0.5% heavy hydrocarbons. Note that in LES, CH_4 is considered as fuel.

combustion chamber via a conical contraction of 18mm (final) diameter into a settling chamber, before passing through a water-cooled back-pressuring valve to the ambient-pressure exhaust duct of the laboratory. As the flow enters this module parallel to the axial centerline of the test-rig, and exits perpendicular to it, we hereafter refer to this section of the chamber as the "turning module" to avoid confusion with the burner plenum, which may also be considered a settling chamber. The rig is equipped with several synchronous experimental diagnostic techniques. The three velocity components in the axial-radial plane of the combustion chamber are measured through a Stereoscopic Particle Image Velocimetry (sPIV) technique. Planar Laser-Induced Fluorescence (PLIF) measurements of OH radicals are also performed to visualize the flame as well as Line-of-Sight (LOS) integration of OH* chemiluminescence that is then used as a qualitative indicator of the heat release rate for lean premixed flames [60]. Pressure is also recorded in the plenum, in the combustion chamber and in the turning module to characterize the flame thermoacoustic response. Measurements of the solid temperature at the centerbody and at the turning module are acquired through thermocouples embedded 5.5 and 2 mm below the surface, respectively. Heat transfer at the combustion chamber walls and at the backplane is estimated from the cooling mass flow rate and the corresponding increase in temperature of the cooling-air. Cooling-air is injected into the turning module after having cooled the combustion chamber quartz walls.

An earlier design iteration of this burner was recently characterized by Slabaugh *et al.* [21] and further analyzed by Zhang *et al.* [22] at elevated thermal power density. Chterev and Boxx [45] were the first to operate the

Case	P [bar]	H_2 [% fuel vol.]	$\dot{m}_{air}$ [g/s]	$\dot{m}_{CH_4}$ [g/s]	$\dot{m}_{H_2}$ [g/s]	T_{inlet} [K]	ϕ	P_{th}
P1H0	1.05	0%	17.6	0.74	-	608	0.71	37KW
P1H40	1.05	40%	17.2	0.62	0.05	590	0.71	37KW
P3H40	3.05	40%	53.7	1.85	0.15	636	0.71	111KW
P5H40	5.02	40%	89.5	3.08	0.26	642	0.71	185kW

Table 1: Summary of the operating conditions considered in the present work.

rig with different levels of hydrogen enrichment to investigate the effect of pressure and hydrogen on the flame dynamics. The operating conditions considered for a global equivalence ratio of $\phi = 0.71$ and a thermal power of P_{th} = 37 kW/bar are summarized in Table 1. Case *P1H0* refers to the condition without hydrogen admixture at atmospheric pressure. Cases *P1H40*, *P3H40* and *P5H40* refer to flames enriched by 40% of hydrogen (by volume) at 1, 3 and 5 bar, respectively.

3. LES setup and modeling challenges

Figure 2 presents the computational domain used for LES with an overview of the unstructured mesh used for Case *P1H0*. The full-length air plenum and the turning module are covered by the simulations. Pressure is directly imposed at the end of the small transverse tube in the turning module to mimic the throttle valve. Rather than meshing the entire internal geometry of the fuel distribution plenum, the fuel injection jets are meshed as a small tubes (shown in red) that extend below the surface of the swirler channels. To help visualize the partially-premixed fuel injection in the swirler, an instantaneous isocontour of CH_4 is also shown in red. The AVBP LES code (cerfacs.fr/avbp7x/index.php) is used to solve the compressible Navier-

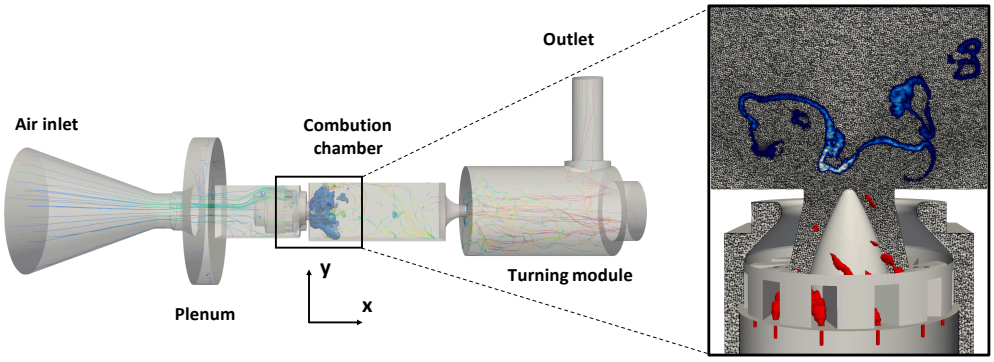

Figure 2: LES computational domain (23M cells) for Case *P1H0*. The full-length air plenum and the turning module are taken into account. Pressure is imposed at the outlet to mimic the throttle valve. The twelve fuel injectors are included in the mesh: an instantaneous isocontour of CH_4 (in red) helps visualize the "technical" injection of fuel. An instantaneous field of heat release rate for Case *P1H0* is also shown in blue in an horizontal plane.

Stokes multi-species equations. The TTGC scheme (third order in time and space) is used to discretize the convective terms [61] while the SIGMA turbulent closure is employed for the LES sub-grid model [62]. In such industrial configurations, flames are usually too thin to be resolved on the numerical grid without asking for unfeasible High Performance Computing (HPC) resources. A solution is then to use the dynamic formulation of the thickening flame model (DTFLES) [63], for which the reactive layer is artificially thickened by reducing the diffusive terms. Since a thickened flame is less sensitive to turbulence, an efficiency function Ξ_Δ is introduced to account for the corresponding reduction of flame surface [61, 64]. A dynamic formulation of the Charlette efficiency function [64] is used here to locally estimate the model parameter β_{Ch} during the simulation, following previous works on the atmospheric PRECCINSTA configuration [65]The CH_4-H_2/Air kinetic scheme

relies on a novel Analytically Reduced Chemistry (ARC) mechanism consisting of 18 transported species, 144 reactions, and 12 quasi-steady state species, derived from the detailed PoliMi scheme [66] using ARCANE [67].This kinetic scheme has been validated through Cantera (www.cantera.org) calculations of a 1D-premixed and 1D-counterflow premixed flames using detailed schemes at elevated pressures (see Supplementary Material). Transport properties are described by a constant mixture Prandtl number and a constant Schmidt number different for each species [68]. Inlet and outlet boundary conditions are modeled with the Navier-Stokes Characteristic Boundary Conditions (NSCBC) [69]. The flow is choked both at the air inlet (through a multi-perforated plate) and at the throttle valve (only at elevated pressure), while the acoustic impedance of the fuel line was reported to have marginal impact on the thermoacoustic oscillation [70]. Following these observations, relaxation coefficients of $K_{air} = 1 \times 10^5$ s^{-1}, $K_{fuel} = 5 \times 10^5$ s^{-1} and $K_{outlet} = 5 \times 10^3$ s^{-1} are imposed on the air inlet, the fuel inlet and the outlet, respectively for the NSCBC method. When it comes to walls, a no-slip condition is used and heat transfer is taken into account by imposing a reference temperature T_{ref} and a suitable thermal resistance R so that, if T_f is the fluid temperature at the wall, the local heat flux Φ_q can be computed as $\Phi_q = (T_f - T_{ref})/R$ [70]. The experimentally measured temperature values for the centerbody and the turning module are used as T_{ref} together with R values that account for the corresponding heat conduction. Complementarily, for the backplane and the combustion chamber walls, T_{ref} is imposed as the average air-cooling temperature and R is tuned to match the experimentally measured heat losses for each operating point. Finally, thermal radiation

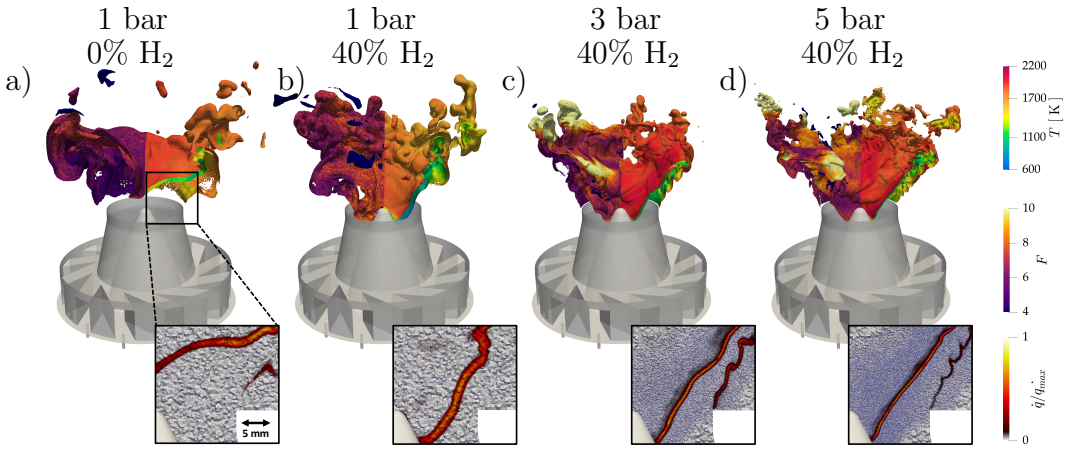

Figure 3: Iso-surfaces of $\dot{q} = 10\%\ \dot{q}_{max}$ colored by thickening field F (on the left) and temperature field T (on the right) for Cases (a) *P1H0* (23M mesh), (b) *P1H40* (23M), (c) *P3H40* (65M) and (d) *P5H40* (144M). A zoom on the flame root showing the grid and the normalized field of heat release rate is also presented. Note that, as a result of the Static Mesh Refinement procedure, a similar thickening field is used for all the flames.

from the hot gases is accounted for through an Optically Thin Assumption (OTA) [71] for the most radiating species CH_4, CO, CO_2, and H_2O. In such a case, gases are assumed to be optically thin and re-absorption is neglected while the Planck mean-absorption coefficients are provided for each species as polynomial functions of temperature [72].

3.1. Modeling challenges at elevated pressure

The LES mesh used for cases *P1H0* and *P1H40* consists of $23M$ tetrahedral cells. This grid has a characteristic size in the flame zone just downstream of the centerbody tip of $\Delta_x = 300\ \mu m$. With this resolution, a y^+ value lower than unity is achieved at the centerbody tip and $y^+ \sim 3$ at the chamber and backplane walls at 1 bar. The reasonably low value of the non-dimensional wall distance hence allows the use of a wall resolved

LES approach and a satisfactory estimation of the thermal boundary layer behavior.

For elevated pressure cases, more attention is to be paid to the LES numerical modeling as pressure (and high power density) modifies the different time scales that characterize these turbulent reactive flows (Table 2). First of all, the Reynolds number significantly increases with pressure [73]. If the exit injector diameter D (i.e. 28 mm) is chosen as characteristic length L and the characteristic velocity u is taken to be the bulk velocity 4 $\dot{m}$ / $\rho\pi D^2$ for all cases to be considered, the Reynolds numbers are 2.7 $\times$ 10^4, 8.1 $\times$ 10^4 and 1.34 $\times$ 10^5 for cases *P1H40*, *P3H40* and *P5H40*, respectively. As a consequence, the smallest turbulent scale, the Kolmogorov length scales η are calculated to be 13.2 μm, 5.8 μm and 4 μm for cases *P1H40*, *P3H40* and *P5H40*, respectively. Note that an increase of pressure from 1 bar to 3 bar halves η while, a further increase to 5 bar only slightly decreases it.

Pressure does not only affect turbulence time scales, it also affects chemical reactions. For an equivalence ratio of 0.71, the laminar flame speed S_L decreases from 1.2 m/s at atmospheric pressure to 0.91 m/s and 0.73 m/s at 3 and 5 bar, respectively. The thermal flame thickness δ_{th} also reduces from 338 μm to 138 and then 96 μm. As a consequence, the chemical time scale τ_c, computed as δ_{th}/S_L, passes from 0.28 ms for Case *P1H40* to 0.15 and 0.13 ms for cases *P3H40* and *P5H40*, respectively.

Thus, both turbulence and chemical time scales are affected by pressure. The ratio between these two time scales controls the flame-turbulence/vortices interaction. The latter can be characterized by two non-dimensional numbers, depending on the turbulent length scale considered, namely the Karlovitz

Case	P [bar]	η [μm]	δ_{th} [μm]	s_L [m/s]	Re [10^4]	Ka [10^2]	Da
P1H40	1.05	13.2	338	1.2	2.7	6.5	8.5
P3H40	3.05	5.8	138	0.91	8.1	5.6	15.7
P5H40	5.02	4	96	0.73	13.4	5.7	18.1

Table 2: Effect of pressure on the turbulent reactive flow time scales. Flame properties are evaluated at the global equivalence ratio of $\phi = 0.71$.

number Ka and the Damköhler number Da [74] that compare the chemical time scale τ_c to the Kolmogorov time τ_k and the integral time scales τ_t, respectively, and can be defined as

$$Ka = \frac{1}{Da\left(\eta_k\right)} = \frac{\tau_c}{\tau_k} = \frac{u'\left(\eta_k\right)/\eta_k}{s_L/\delta} = \left(\frac{\delta}{\eta_k}\right)^2, \tag{1}$$

$$Da = Da\left(l_t\right) = \frac{\tau_t}{\tau_c} = \frac{l_t/u'\left(l_t\right)}{\delta/s_L}. \tag{2}$$

The Karlovitz number compares the the smallest turbulent time scales and the chemical time scale: it indicates whether the Kolmogorov scale structures are able to penetrate and thereby modify the inner flame sheet. Computing Ka (Table 2) reveals that pressure only slightly affects the Karlovitz number and hence the interaction between the Kolmogorov scale and the flame front because both Kolmogorov scale η (τ_k) and flame thickness δ (τ_c) decrease with pressure. Therefore, pressure does not modify the interactions between the small turbulent scales and the flame. The Damköhler number, instead, describes the interaction between large vortical structures and the flame front by comparing the integral time scale to the chemical one. To compute the Damköhler number, the integral time scale τ_t, which is a characteristic flow time τ_{flow}, can be taken for example as the period of the

combustion chamber first acoustic mode (i.e. f = 420 Hz, $\tau_t = 2.38$ ms) that corresponds to the longest flame dynamics time scale [75]. In that case, the Damköhler number goes from a value of 8.5 at atmospheric pressure to 15.7 and 18.1 for 3 and 5 bar, respectively (Table 2). Indeed, since the flow characteristic time and the large vortical structure remain essentially the same, due to the reduction in the chemical time scale, the Damköhler number increases with pressure.

The decrease in timescales of both turbulence and chemistry with increasing pressure, and concomitant increase in Damkohler number over the range of conditions poses a clear challenge for LES to properly capture such changes and mesh requirements become rapidly demanding. Here, a comparison of predictions with a model as TFLES requires in principle the same relative thickening of the various flame fronts and hence grid adaptation. To properly increase resolution, a Static Mesh Refinement (SMR) is introduced to refine the grid for cases *P3H40* and *P5H40* so that the same artificial thickening and hence the same combustion modeling for all flames is produced [76]. Prescribing a thickening goal of $F \sim 8$, the procedure leads to grids of 65M cells and 144M cells for Cases *P3H40* and *P5H40*, respectively. The increase in cells number is not linear with the reduction in δ_{th} but increases with its cube when pressure goes up. Hence, the observed increase in cells number underlines the need for HPC resources when dealing with elevated pressure combustors if requiring reasonable resolution of the flame front.

Figure 3 presents iso-surfaces of heat release rate $\dot{q} = 10\%\ \dot{q}_{max}$ colored by the thickening field F (on the left) and temperature T (on the right) for (a) Case *P1H0* (23M mesh), (b) Case *P1H40* (23M), (c) Case *P3H40* (65M)

and (d) Case *P5H40* (144M). A zoom on the flame root showing the grid and the normalized field of heat release rate $\dot{q}/\dot{q}_{max}$ is also presented to visualize the resolution of the flame front. As expected, due to the use of SMR, a similar instantaneous thickening field is obtained while resolving all flames. The flame thickness significantly reduces when increasing both pressure and hydrogen enrichment levels.

4. Hydrogen effect at atmospheric pressure

Experimental measurements and LES predictions of the reference Case *P1H0* (1 bar, 0% H_2) and Case *P1H40* (1 bar, 40% H_2) are discussed now to highlight the impact of hydrogen enrichment at atmospheric pressure. First, H_2 addition effect on the flame shape and stabilization is discussed (section 4.1). Then, the thermoacoustic response and the flame dynamics are analyzed (section 4.2).

4.1. Flame shape and stabilization

Figure 4(a-b) presents the experimentally measured time-averaged LOS-integrated OH* chemiluminescence image compared to the LOS predicted heat release rate $\overline{\dot{q}}$ for (a) Case *P1H0* and (b) Case *P1H40*, respectively. For the reference case without hydrogen (Fig. 4(a)) the flame takes on a lifted M-shape both in experiments and LES. In good agreement with the experimentally measured OH* chemiluminescence signal, the Outer Recirculation Zones (ORZ) do not show any heat release rate. In contrast, when 40% hydrogen enrichment is added to the fuel, the flame takes on a V-shape. It attaches to the centerbody tip and the flame length reduces, Fig. 4(b).

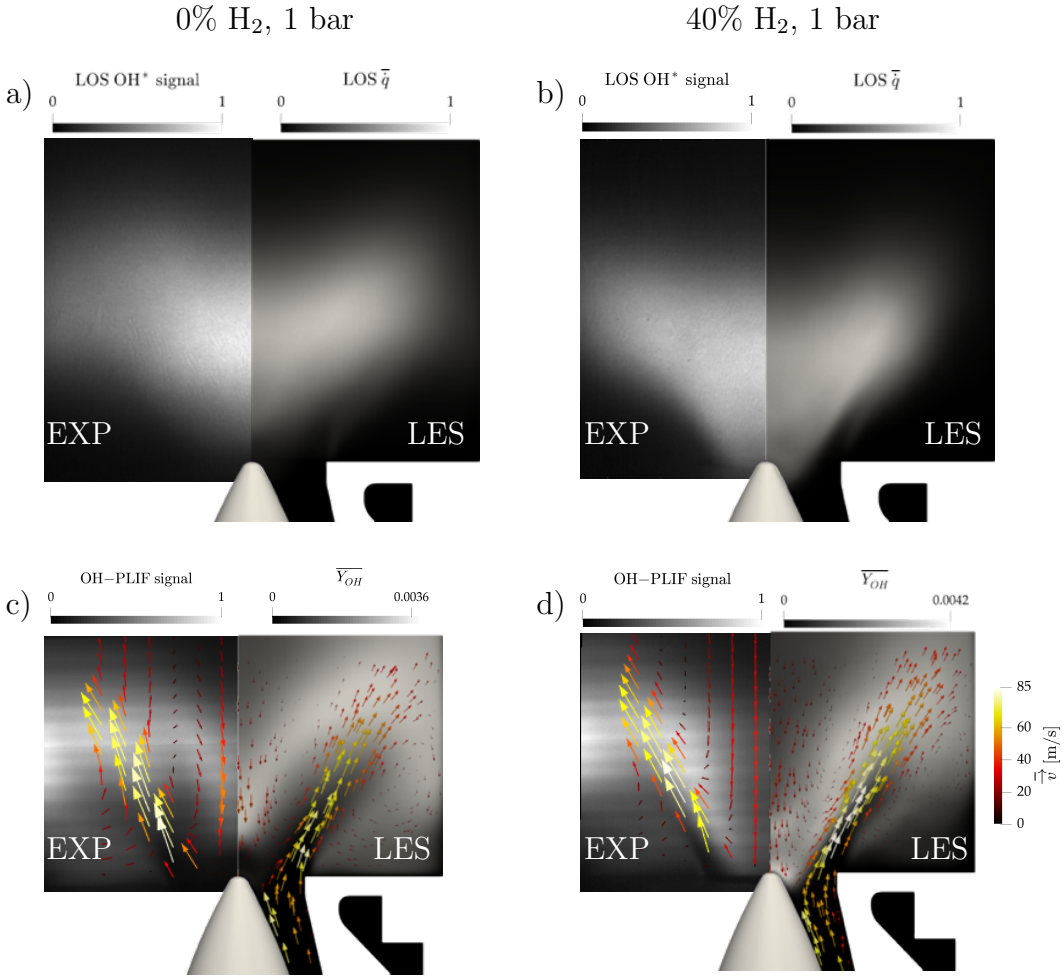

Figure 4: Experimentally measured time-averaged LOS-integrated OH* chemiluminescence image and time-averaged OH-PLIF signal compared to predicted LOS heat release rate $\bar{\dot{q}}$ and OH mass fraction $\overline{Y_{OH}}$ for Cases (a-c) *P1H0* and (b-d) *P1H40*, respectively. The arrows are tangential to the measured and computed time-averaged velocity field in the plane $\overline{\vec{v}_{//}}$. Their length and color indicate the velocity magnitude.

The shape change also appears in the experimentally measured time-averaged OH-PLIF signal compared to the computed OH mass fraction [2]

[2]Note that the measured OH-PLIF signal is here considered to be proportional to OH mass fraction as a first approximation. However, more generally, OH-PLIF is not a direct

$\overline{Y_{OH}}$ in Fig. 4(c-d) for Case *P1H0* and Case *P1H40*, respectively. The arrows are tangential to the experimentally measured and numerically computed time-averaged velocity field in the plane $\overline{\vec{v}_{/\!/}}$, the length and color of the vector indicating the velocity magnitude. Both in experiments and LES, no OH signal is observed close to the centerbody tip in the reference case, confirming that the flame is not attached to the centerbody walls, Fig. 4(c). However, OH is present in the ORZs, pointing to high temperatures in these specific regions. No OH is detected in the high velocity region at the injector exit. For this case, LES correctly predicts both the flame shape and its stabilization process/location as well as the velocity field experimentally measured (quantitative comparison is provided in the Supplementary Material).

When hydrogen is added to the fuel mixture, the flame assumes a V-shape, with flame roots well attached to the centerbody tip, as indicated by the high values of OH signal on Fig. 4(d). In contrast to Case *P1H0*, the CRZ shows lower OH signal while the OH mass fraction peak value is notably higher [77]. Again, LES correctly predicts the experimental velocity field (a quantitative comparison is provided in the Supplementary Material) and the flow acceleration due to the increased combustion intensity while no OH is observed in the high velocity region at the injector exit. The flame is now able to stabilize at the centerbody tip walls in the shear layer region. This change is due to the increased laminar flame speed (see Supplementary Material) and the higher resistance to strain-induced extinction of hydrogen enriched flames [78].

measure of OH number density since measurements can be affected, among others, by pressure, quenching, laser and signal absorption.

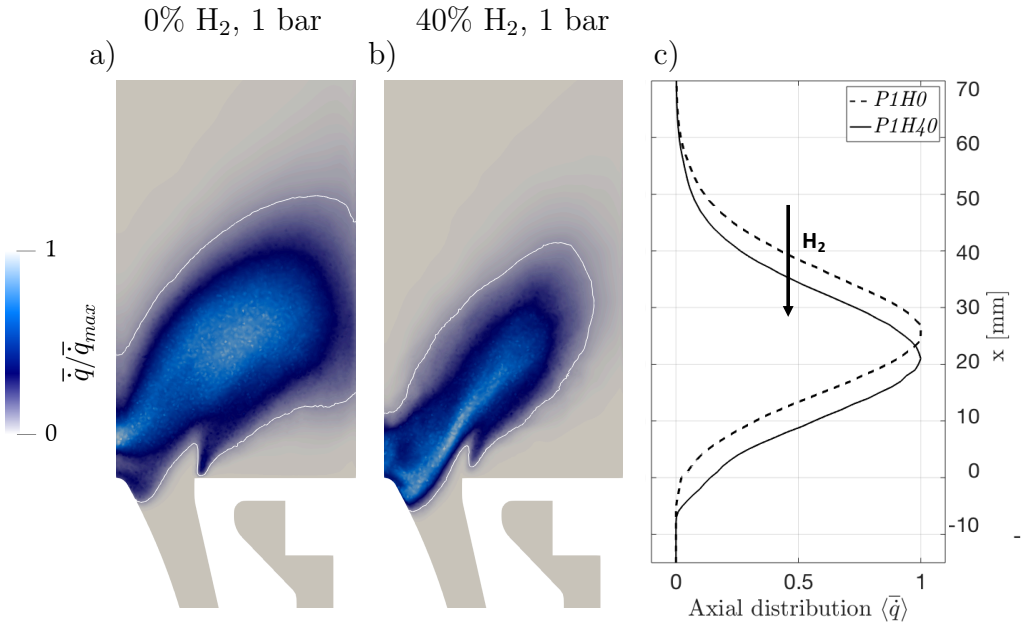

Figure 5: Normalized time-averaged heat release rate $\dot{\bar{q}}/\dot{\bar{q}}_{max}$ predicted via LES for Cases (a) *P1H0* and (b) *P1H40*. (c) Mean axial distribution $\langle\dot{\bar{q}}\rangle$. White isocontours indicate 10% of $\dot{\bar{q}}_{max}$.

A more direct comparison of flame shapes and stabilization is provided in Fig. 5. To do so, the normalized time-averaged heat release rate $\dot{\bar{q}}/\dot{\bar{q}}_{max}$ predicted via LES is shown for both (a) Case *P1H0* and (b) Case *P1H40*, the added white isocontours indicating 10% of $\dot{\bar{q}}_{max}$. The reference flame (Fig. 5(a)) shows a lifted M-shape. It is longer and the heat release rate reaches the side chamber walls. A strong heat release rate region is observable along the axis, downstream of the centerbody tip. Regions of low heat release rate are found near the centerbody wall and at the backplane corner, indicating that the flame is sporadically present in these regions while never being fully stabilized. In contrast, (b) Case *P1H40* shows that the flame root is firmly stabilized at the centerbody wall, as confirmed by the large values of heat release rate. A blurry region of $\dot{\bar{q}}$ is noticeable downstream of

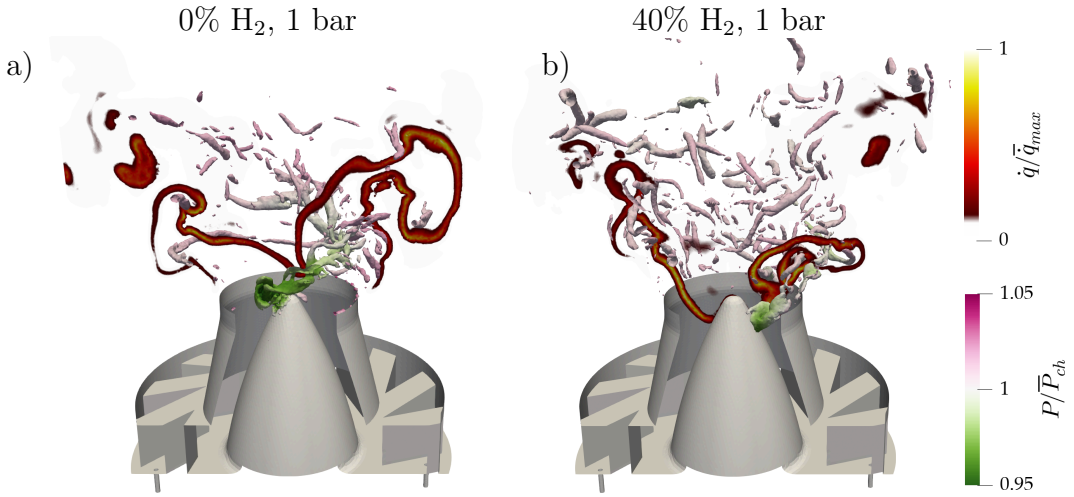

Figure 6: Comparison of instantaneous isosurface of Q-criterion at Q = 280 $\overline{U_x^2}/D_{inj}^2$ colored by pressure and field of instantaneous normalized heat release rate $\dot{q}/\dot{q}_{max}$ for Cases (a) *P1H0* and (b) *P1H40*.

the centerbody tip, suggesting that, from time to time, flame branches are present in this region. The flame tip is now positioned farther away from the side chamber walls, the flame being shorter.

To achieve a more quantitative comparison, the normalized time-averaged heat release rate fields are integrated over the combustor cross section S_c. In such a case, one-dimensional mean axial distributions $\langle\overline{\dot{q}}\rangle$ are obtained for both cases in Fig. 5(c), as expressed by

$$\langle\overline{\dot{q}}\rangle(x) = \frac{1}{S_c}\iint_{S_c}\overline{\dot{q}}(x,y,z)dydz. \tag{3}$$

The effect of hydrogen enrichment on the flame stabilization and length is evident. When 40% hydrogen admixture is considered, both the peak of heat release rate and the flame stabilization point are shifted upstream by approximately 10 mm: the flame is more compact.

Visualization of the unsteadiness in a flow-field can be conveyed and illustrated through an instantaneous view of the Q-criterion identifying the presence of coherent vortical structures [79]. Figure 6 compares a Q-criterion isosurface at Q = 280 $\overline{U_x^2}/D_{inj}^2$ colored by pressure superimposed to a field of instantaneous normalized heat release rate $\dot{q}/\dot{q}_{max}$ for (a) Case *P1H0* and (b) Case *P1H40*. Both cases show the presence of a Precessing Vortex Core (PVC) [45], identified through a low pressure value (colored in green). The lifted M-flame presents a strong PVC that impacts the flame downstream of the centerbody tip. The PVC is still present when the flame assumes a V-shape, as opposed to what was generally observed in the atmospheric PRECCINSTA burner in which V flames are usually found to suppress the formation of the PVC. However, as experimentally observed [45], the PVC strength is significantly reduced, as indicated by the volume taken by the green Q-criterion isosurface. Despite this change, the PVC is still able to interact and distort the flame branches, causing the widened heat release rate region downstream of the centerbody in Fig. 5(b). We observe no particular difference in terms of dimensions between these two cases when it comes to the vortical structures detaching from the backplane, indicating that the flame shape does not significantly impact the flow topology in the outer flow region.

4.2. Thermoacoustic response and flame dynamics

Figure 7 presents the (a) experimentally measured and (b) LES-predicted fluctuations of pressure in the combustion chamber (black), plenum (blue) and turning module (gray) for Case *P1H0*. The red line reports (a) the experimental volume-integrated OH* chemiluminescence signal and (b) the

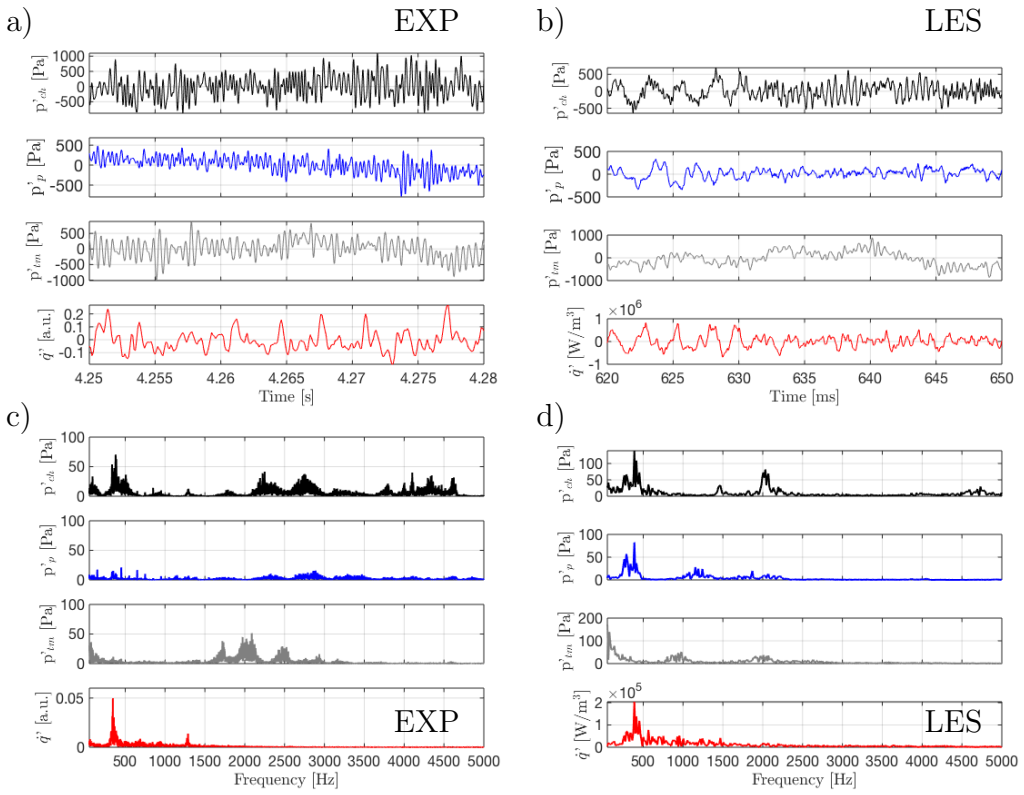

Figure 7: (a) Experimentally measured and (b) LES-predicted fluctuations of pressure in the combustion chamber (black), plenum (blue) and turning module (gray). The red line reports (a) volume-integrated OH* chemiluminescence signal and (b) heat release rate. (c-d) Signals spectra. Case *P1H0*: 0% H_2, 1 bar.

numerically predicted heat release rate. Both in experiments and LES, pressure oscillation levels in the combustion chamber, plenum and turning module reach approximately 1000 Pa. Fluctuation of OH* chemiluminescence signal and heat release rate are weak and do not strongly correlate with pressure fluctuations in the combustion chamber. Corresponding spectra are presented in Fig. 7(c-d) for the experiments and LES, respectively. The pres-

sure spectrum in the combustion chamber shows a weak peak at 380 Hz (80 Pa) and broad band noise in the high frequency range, above 2000 Hz. LES predicts a small peak at 390 Hz and also noise in the high frequency range. Note that some activity is present in the turning module at this high frequency range, suggesting that the noise registered is likely linked to acoustic modes of the turning module. OH* chemiluminescence and heat release rate spectra also exhibit the same peaks around 380 Hz both in experiments and LES, suggesting a weak coupling between heat release rate fluctuation and chamber pressure. However, the pressure fluctuation levels at this frequency in the combustion chamber (80 Pa) can be considered small compared to the global level of pressure fluctuation (i.e. 1000 Pa), indicating that no significant thermoacoustic activity is present. One can finally underline the presence in the experimentally measured OH* chemiluminescence spectrum of a small peak at 1280 Hz which corresponds to the PVC frequency as reported by Chterev and Boxx [45].

When 40% hydrogen admixture is considered, the flame thermoacoustic response changes significantly. Figure 8 presents the (a) measured and (b) computed oscillations of pressure in the combustion chamber (black), plenum (blue) and turning module (gray) for Case *P1H40*. The red line reports (a) the volume-integrated OH* chemiluminescence signal and (b) the LES-predicted heat release rate. While pressure oscillations in the plenum and in the turning module are of the same order of magnitude as for the reference case, pressure fluctuations in the combustion chamber are notably higher both in the experiments and LES (i.e. 2 kPa). Furthermore, the OH* chemiluminescence and the heat release rate signals oscillate in a coherent

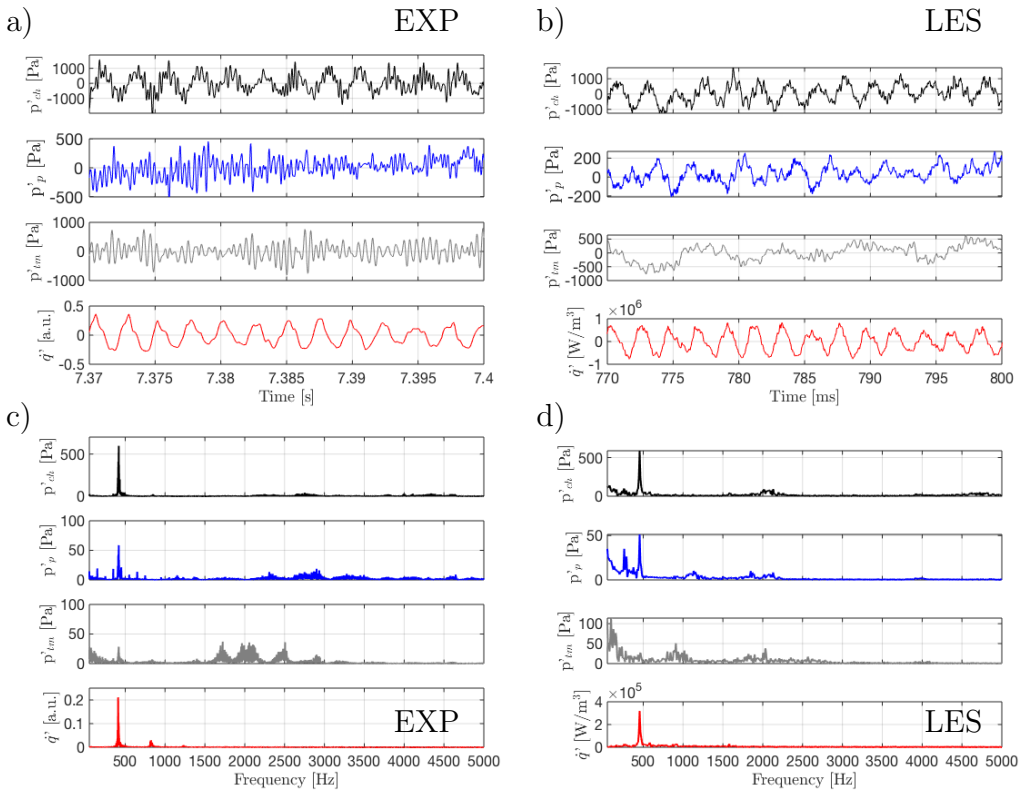

Figure 8: (a) Experimentally measured and (b) LES predicted fluctuations of pressure in the combustion chamber (black), plenum (blue) and turning module (gray). The red line reports (a) volume-integrated OH* chemiluminescence signal and (b) heat release rate. (c-d) Signals spectra. Case *P1H40*: 40% H_2, 1 bar.

way and seem to be correlated to the pressure fluctuation in the combustion chamber. Corresponding measured and computed spectra are shown in Fig. 8(c-d), respectively: experimental measurements show strong peaks in the combustion chamber pressure (600 Pa) as well as in the OH* chemiluminesce spectra at 420 Hz, indicating that a thermoacoustic activity is present when 40% hydrogen enrichment is considered. LES correctly predicts the

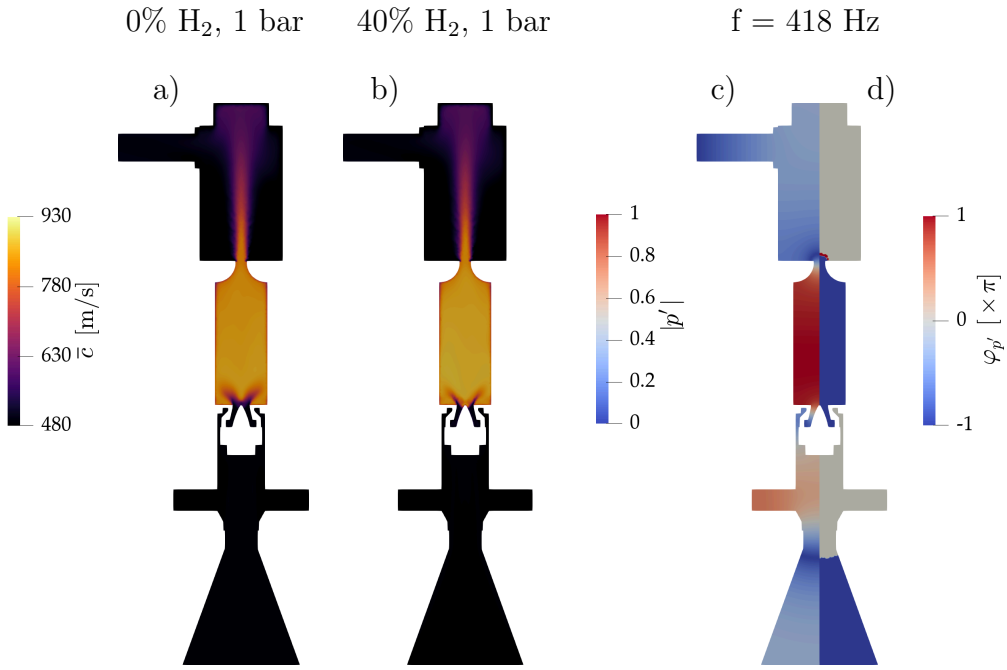

Figure 9: LES-predicted time-averaged sound speed field $\bar{c}$ for Cases (a) *P1H0* and (b) *P1H40*. (c) Amplitude and (d) phase of the first acoustic (chamber) mode at 418 Hz computed with the Helmholtz solver for Case *P1H40*.

thermoacoustic limit-cycle at 440 Hz, as well as the proper pressure chamber oscillation level (600 Pa). Experimentally, high frequency noise is still observed in the turning module but is no longer recorded in the combustion chamber.

To investigate the nature of this thermoacoustic activity, the AVSP Helmholtz solver [80] is used to compute the acoustic modes of the system. To do so, the LES-predicted time-averaged sound speed fields $\bar{c}$, shown in Fig. 9 of (a) Case *P1H0* and (b) Case *P1H40*, are used as an input to the Helmholtz solver. Adding H_2 only slightly impacts the mean temperature field, leading to weak differences in the corresponding time-averaged sound speed fields. As a consequence, the first acoustic mode of the system shows negligible differences in terms of mode shape and frequency. One acoustic mode is found

at a frequency close to the peak recorded for Case *P1H40*: i.e. 420 Hz. This mode, predicted at 418 Hz by LES, corresponds to a 3/4 wave (chamber) mode[3].

Dynamics of the H_2-enriched flame during the thermoacoustic oscillation is shown in Fig. 10 through instantaneous fields of the experimentally measured OH-PLIF signal (top), LES-predicted OH mass fraction Y_{OH} (middle) and hydrogen mass fraction Y_{H_2} (left, bottom) as well as the flow normal vorticity to the visualized plane $\omega_\perp$ (right, bottom). Red and white isocontours refer respectively to the heat release rate $\dot{q}$ at 10% of $\dot{q}_{max}$ and a low pressure value. Four equivalent phases are considered during the thermoacoustic oscillation for the experiments and LES. Instants (a) and (c) correspond respectively to the maximum and the minimum of OH* chemiluminescence and heat release rate signals while instants (b) and (d) correspond to a phase difference of $\pi/2$. Both experimentally, Fig. 10(top), and numerically, Fig. 10(middle), a classical flame response to a longitudinal mode is observed. The flame eventually detaches from the centerbody walls at instant (a), when the heat release rate is maximum, flame surface being notably smaller at instant (c), when the heat release rate is minimum. The stabilization point of the flame

[3]In the Helmholtz solver, a velocity node has been imposed for the air and fuel inlets as acoustic boundary conditions since flow is choked through small holes at the air inlet and acoustic BCs at the fuel inlet does not play a significant role [70]. A pressure node has been imposed at the turning module outlet, since at atmospheric condition the outlet valve is not choked. Note also that the Mach number at the combustion chamber nozzle exit is of the order of 0.5 but the AVSP Helmholtz solver is a zero Mach code so it does not take into account mean flow velocity and compressibility effects in the computation of the acoustic modes.

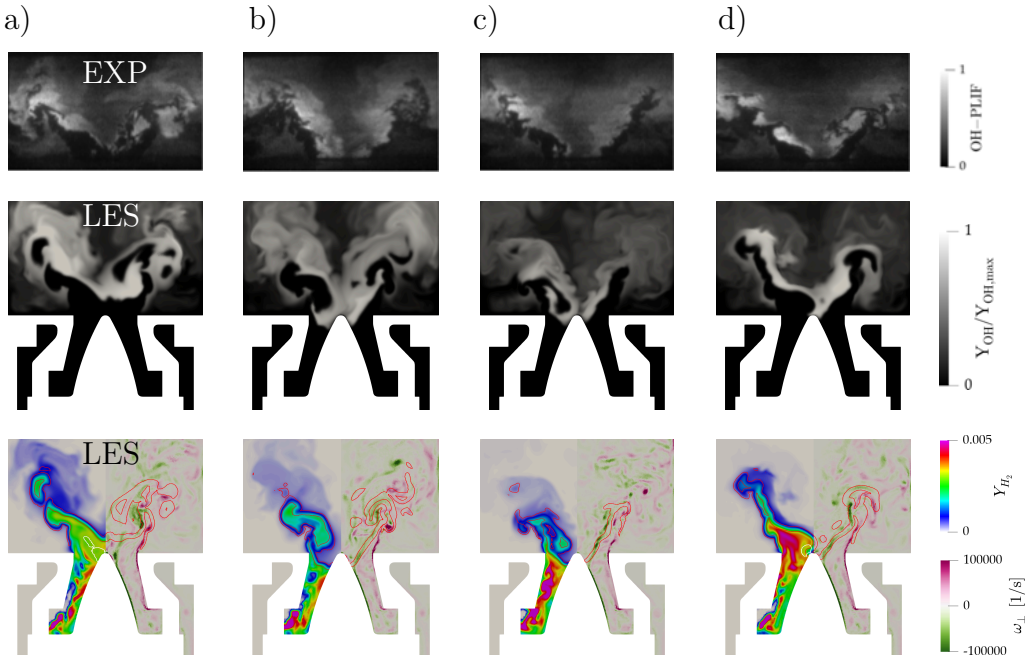

Figure 10: Instantaneous fields during the thermoacoustic oscillation of : experimentally measured OH-PLIF signal (top), LES-predicted OH mass Y_{OH} (middle) and hydrogen mass fraction Y_{H_2} (left, bottom) and flow vorticity normal to the plane $\omega_\perp$ (right, bottom). Red and white isocontour refer to with heat release rate $\dot{q}$ at 10% of $\dot{q}_{max}$ and low pressure respectively. Four equivalent instants are considered during the thermoacoustic oscillation for experiments and LES. Instants (a) and (c) correspond to a maximum and a minimum respectively in the volume-integrated OH* chemiluminescence signal and the predicted heat release rate. Case *P1H40*: 1 bar, 40% H_2.

does move considerably during the thermoacoustic oscillation. As observed in Fig. 10(bottom), fuel-rich pockets are released in the combustion chamber and produce equivalence ratio fluctuations: a mechanism similar to the one observed in the original atmospheric-pressure version of the PRECCINSTA burner [81]. At the same time, (d) the interaction between the vortical structures detaching from the backplane corner and the flame is observable as well as the (d) flame front distortion due to the PVC (highlighted by the

low-pressure white isocontour). The latter explains the wide heat release rate region visible along the axis of the domain shown in Fig. 5(b), the PVC being able to drag the flame front toward the region downstream of the centerbody tip.

5. Elevated pressure effect

Measurements and computations of Case *P3H40* (3 bar, 40% H_2) and Case *P5H40* (5 bar, 40% H_2) are hereafter presented and compared to Case *P1H40* (1 bar, 40% H_2), showing the impact of elevated pressure on hydrogen enriched flames. The effect on the flame shape and its stabilization is discussed in section 5.1 while the change in the flame thermoacoustic response is analyzed in section 5.2. Finally, a discussion on the reactive flow time scales at different pressures is provided in section 5.3.

5.1. Flame shape and stabilization

Figure 11(a-c) compares the time-averaged LOS-integrated OH* chemiluminescence image to the LOS-integrated heat release rate $\overline{\dot{q}}$ computed via LES for (a) Case *P1H40*, (b) Case *P3H40* and (c) Case *P5H40*, respectively. While the 1 bar H_2-enriched flame (Fig. 11(a)) presents a V-shape attached to the centerbody tip as observed in section 4.1, the 3 bar and the 5 bar cases (Fig. 11(b-c), respectively) present an attached M-shape for which the flame is anchored both at the centerbody tip and at the backplane. As pressure increases from 1 to 3 bar, the flame length and angle are significantly reduced while, a further increase in pressure to 5 bar only slightly modifies the flame shape. The time-averaged OH-PLIF images are compared to the computed OH mass fraction $\overline{Y_{OH}}$ in Fig. 4(c-e) for (a) Case *P1H40*, (b) Case *P3H40* and

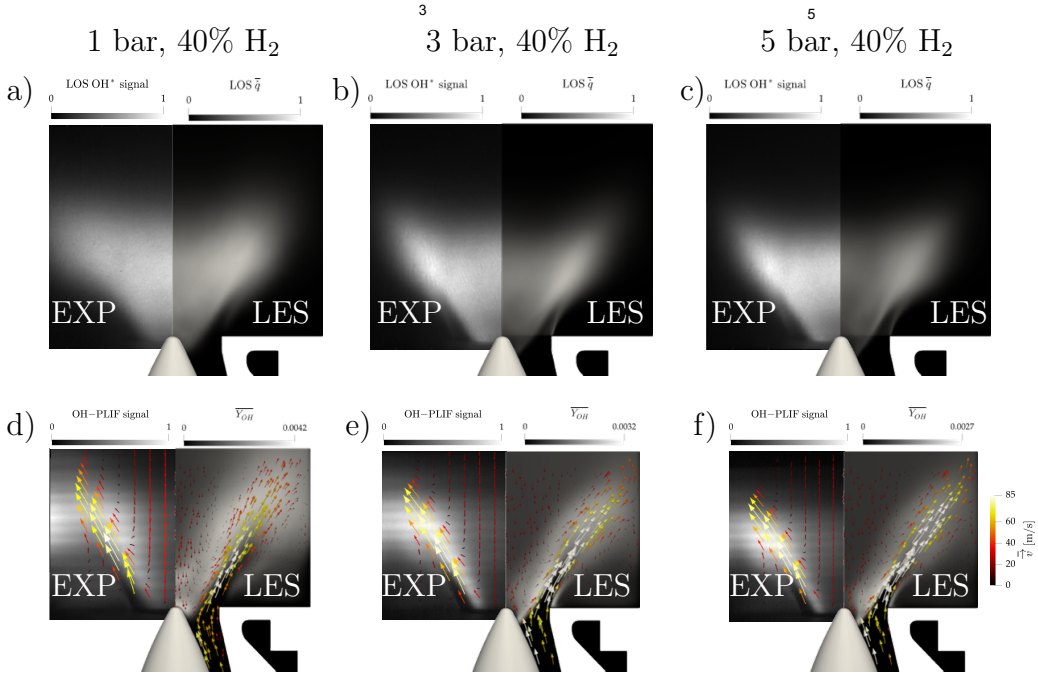

Figure 11: Experimentally measured time-averaged LOS-integrated OH* chemiluminescence image and time-averaged OH-PLIF signal compared to predicted LOS heat release rate $\bar{\dot{q}}$ and OH mass fraction $\overline{Y_{OH}}$ for cases (a-d) *P1H40*, (b-e) *P3H40* and (c-f) *P5H40*, respectively. The arrows are tangential to the measured and computed time-averaged velocity field in the plane $\overrightarrow{\overline{v}}_{//}$. Their length and color indicate the velocity magnitude.

(c) Case *P5H40*, respectively. The arrows provide a qualitative comparison between the experimentally measured and the LES-predicted velocity field in the plane $\overrightarrow{\overline{v}}_{//}$, their length and color indicating the velocity magnitude (quantitative validation being available in the Supplementary Material). Both in experiments and LES, increasing pressure leads to a reduction in the extent of the OH field: while at atmospheric pressure it reaches the view's limit, at 3 and 5 bar the height is decreased. At the same time, OH is increasingly present in the ORZs as the pressure increases, due to the secondary flame

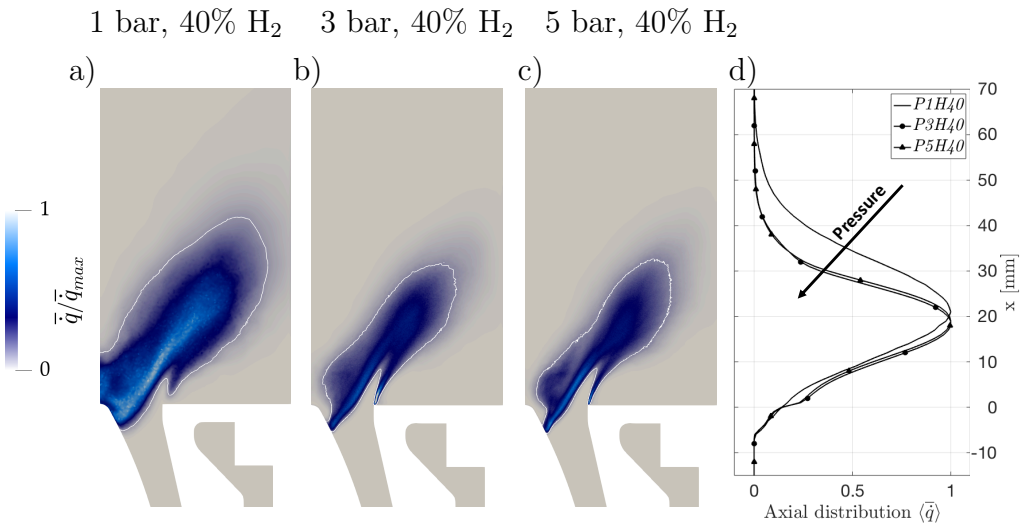

Figure 12: Normalized time-averaged heat release rate $\overline{\dot{q}}/\overline{\dot{q}}_{max}$ predicted via LES for Cases (a) *P1H40*, (b) *P3H40* and (c) *P5H40*. (d) Mean axial distribution $\langle\overline{\dot{q}}\rangle$. White isocontours indicate 10% of $\overline{\dot{q}}_{max}$.

branches that appear to be closer to the backplane corner at 3 and 5 bar. In none of the three cases OH is detected in the high velocity region at the injector exit. Note that the peak value of OH concentration predicted via LES decreases with increasing pressure. This reflects the strong pressure-dependence of OH-species lifetime, which is driven primarily through by the rate of 3-body molecular collisions in the system. Note also that the OH signal just downstream of the centerbody tip decreases with pressure. Overall and for all cases, LES is found to be in satisfactory agreement with experimentally measured quantities and it correctly reproduces the shape change from a V-flame toward an attached M-flame with a corresponding reduction in length with elevated pressure. The latter is likely due to the decrease in chemical time scale (and hence increase in reactivity) for high pressure flames (see section 5.3).

Figure 12 presents the normalized time-averaged heat release rate $\overline{\dot{q}}/\overline{\dot{q}}_{max}$

predicted via LES for (a) Case *P1H40*, (b) Case *P3H40* and (c) Case *P5H40*, while the white isocontour represents the 10% of $\overline{\dot{q}}_{max}$. The flame at atmospheric pressure (Fig. 12(a)) clearly shows a V-shape attached at the centerbody while (b) Case *P3H40* and (c) Case *P5H40* show a M-shape attached both at the centerbody tip and at the backplane. As the flame transits towards a M-shape, it becomes more compact as seen in Fig. 12(d) which presents the one-dimensional mean axial distribution of heat release rate $\langle\overline{\dot{q}}\rangle$, while the stabilization point at the centerbody wall does not change. The heat release rate distribution significantly changes when passing from 1 to 3 bar. However, it remains essentially the same when further increasing the pressure to 5 bar.

5.2. Thermoacoustic response

As pressure increases, the thermoacoustic response of the flame changes. Figure 13 presents (a) the measured and (b) the computed oscillations of pressure in the combustion chamber (black), plenum (blue) and turning module (gray) for Case *P3H40*. The red line corresponds to (a) the volume-integrated OH* chemiluminescence signal and (b) the computed heat release rate. Both in experiments and LES, pressure oscillation levels in the combustion chamber and plenum are of the order of 2 kPa while experimentally the turning module exhibits epochs of large pressure fluctuations of approximately 10 kPa. Fluctuations of OH* chemiluminescence and heat release rate are however weak and not correlated to pressure fluctuations in the combustion chamber. To confirm this observation, corresponding spectra are presented in Fig. 13(c-d) for the experiments and LES, respectively. As the power density increases due to pressure increase, more modes are excited and different

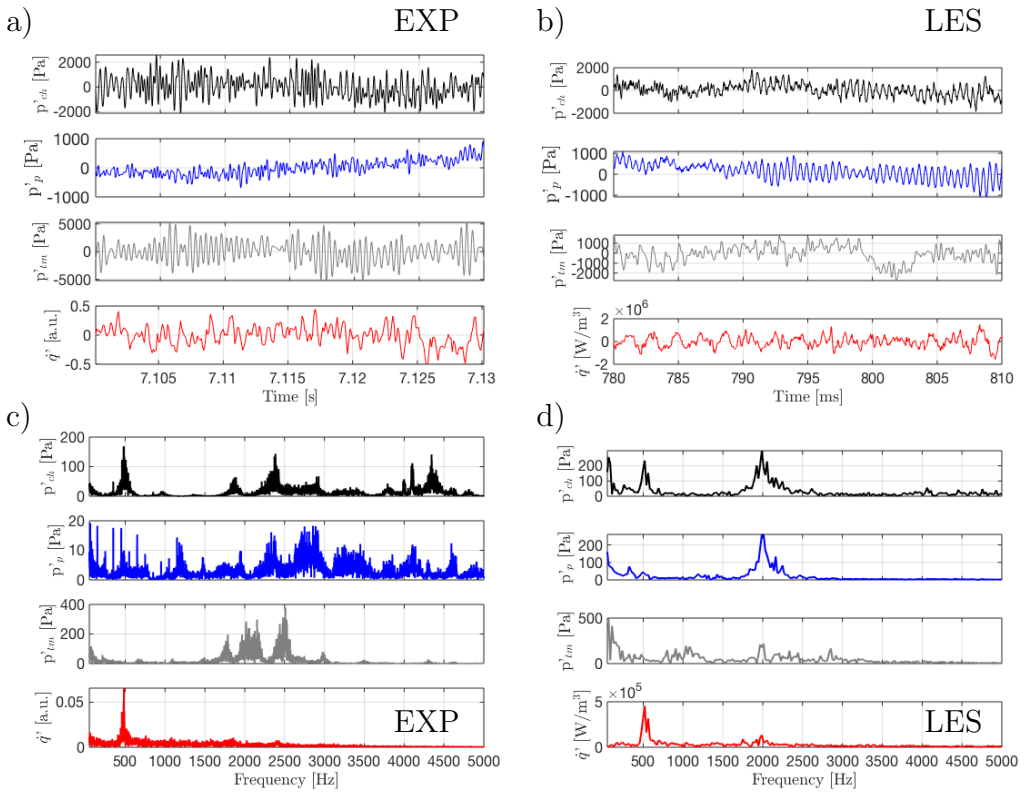

Figure 13: (a) Experimentally measured and (b) LES-predicted fluctuations of pressure in the combustion chamber (black), plenum (blue) and turning module (gray). The red line reports (a) volume-integrated OH* chemiluminescence signal and (b) heat release rate. (c-d) Signals spectra. Case *P3H40*: 40% H_2, 3 bar.

peaks appear in the spectra. Recorded pressure in the combustion chamber shows a weak peak at 483 Hz (150 Pa) that is predicted via LES near 510 Hz. The same peaks appear in both the OH* chemiluminescence and heat release rate spectra, suggesting a weak thermoacoustic coupling at these frequencies. The pressure fluctuation amplitude in the combustion chamber remains small and this Case *P3H40* can be considered as stable, i.e. with no

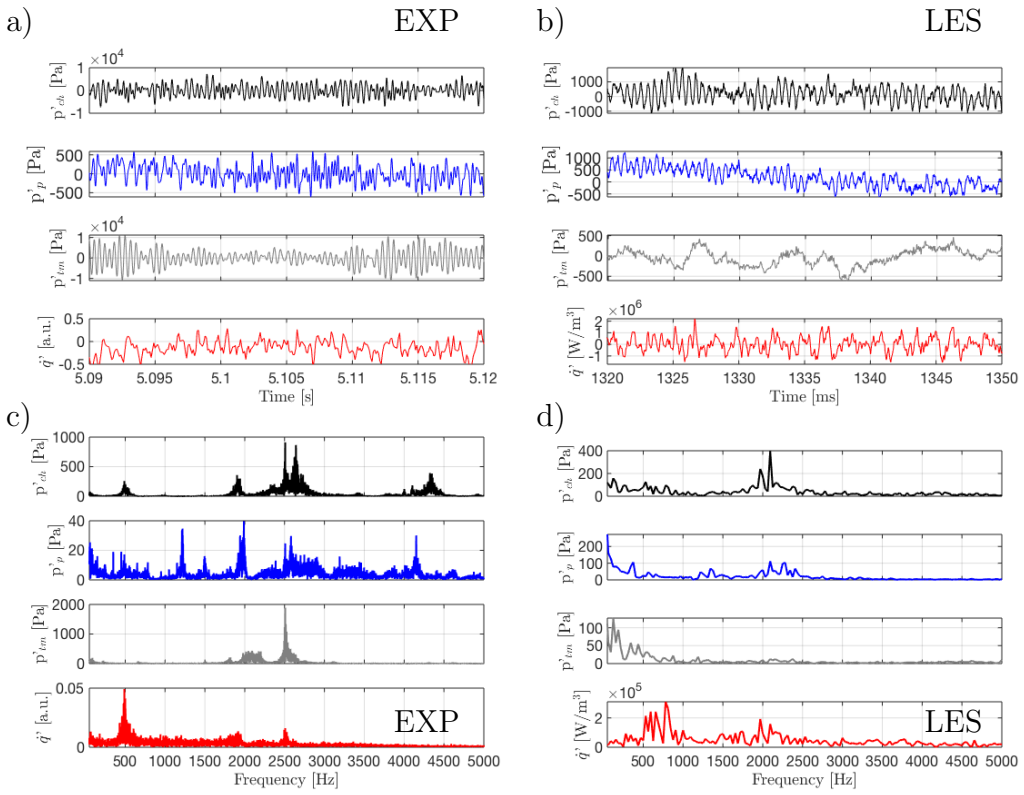

Figure 14: (a) Experimentally measured and (b) LES predicted fluctuations of pressure in the combustion chamber (black), plenum (blue) and turning module (gray). The red line reports (a) volume-integrated OH* chemiluminescence signal and (b) heat release rate. (c-d) Signals spectra. Case *P5H40*: 40% H_2, 5 bar.

strong thermoacoustic activity. Broad band noise with some peaks at higher frequencies are however visible in the chamber, turning module and plenum. This time, since the low frequency mode is weaker compared to Case *P1H40*, the high frequency range noise is more evident, similarly to Case *P1H0*.

A similar thermoacoustic response is observed at 5 bar. Figure 13 shows (a) the measured and (b) computed pressure fluctuations in the combustion

chamber (black), plenum (blue) and turning module (gray) for Case *P5H40*. The OH* chemiluminescence and heat release rate signals are shown in red in Fig. 13(a-b), respectively. As pressure is further increased, the pressure oscillation amplitude in the chamber, plenum and turning module increase both in the experiments and LES while the heat release rate and the OH* chemiluminescence oscillations are seen to be not in phase with the pressure chamber fluctuation. Corresponding spectra in Fig. 13(c-d) confirm this observation and underline that, as pressure increases, the high frequency noise intensity gets larger while the low frequency range oscillations remain small. OH* chemiluminescence and heat release rate spectra do show small peaks at 490 Hz and 530 Hz respectively, but the importance of the pressure oscillation in the combustion chamber at these frequencies remains negligible (200 Pa) compared to the global level of pressure fluctuations: this case can again be considered as thermoacoustically stable. Pressure is therefore found to consistently reduce the thermoacoustic oscillation in the low frequency range while increasing the high frequency activity although it does not couple with the heat release rate fluctuation.

This different thermoacoustic response can be due either to the flame shape change induced by the elevated pressure or to a change in the acoustic modes of the system. The latter mainly depends on the mean temperature field (that in turns affects the sound speed field) and on the acoustic boundary conditions. Figure 15 presents the computed time-averaged sound speed field $\overline{c}$ for (a) Case *P1H40*, (b) Case *P3H40* and (c) Case *P5H40* and clearly disqualifying such a process. In the elevated pressure cases, the turning module outlet valve is choked, meaning that it acoustically behaves like a

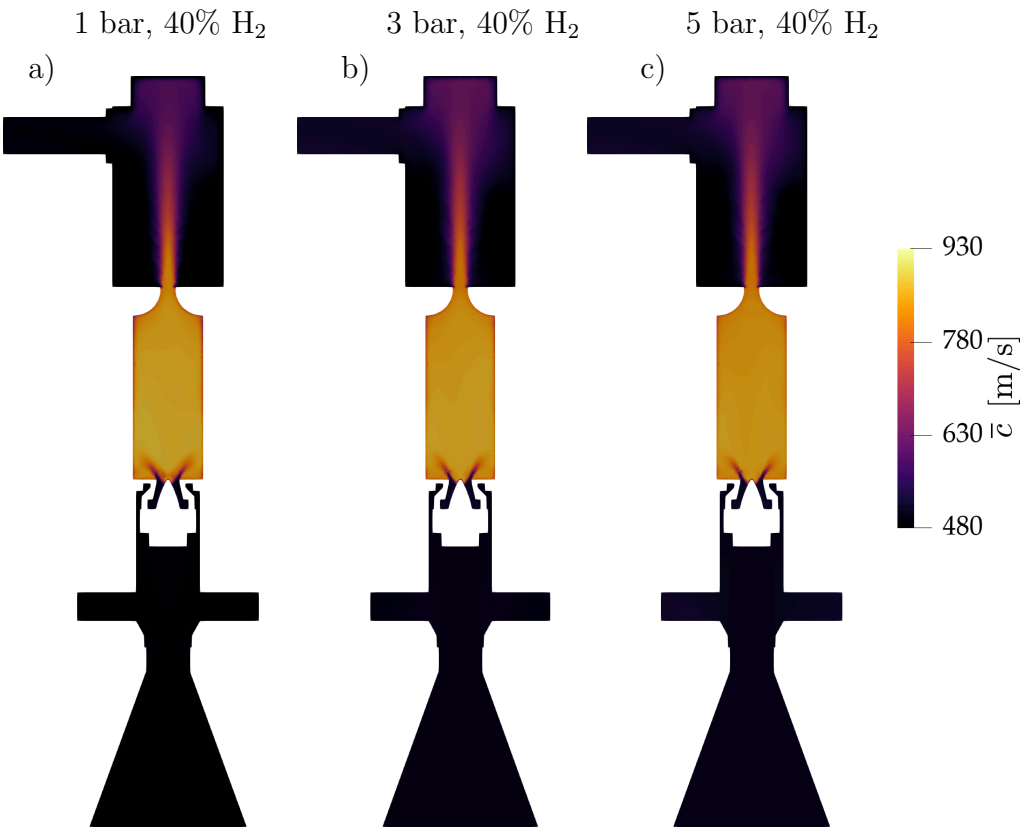

Figure 15: LES-predicted time-averaged sound speed field $\bar{c}$ for Cases (a) *P1H40*, (b) *P3H40* and (c) *P5H40*.

wall (i.e. zero velocity fluctuation), which is not the case at atmospheric pressure. In such a case, the AVSP computation resulted in only a slight increase of the mode frequency, i.e. from 418 Hz at 1 bar to 432 Hz at 5 bar. Therefore, the effect of pressure on the system acoustic modes in the low frequency range is negligible and the change in the flame thermoacoustic response at elevated pressure is likely due to the changes in the flame shape and, hence, its response to acoustic oscillations [82].

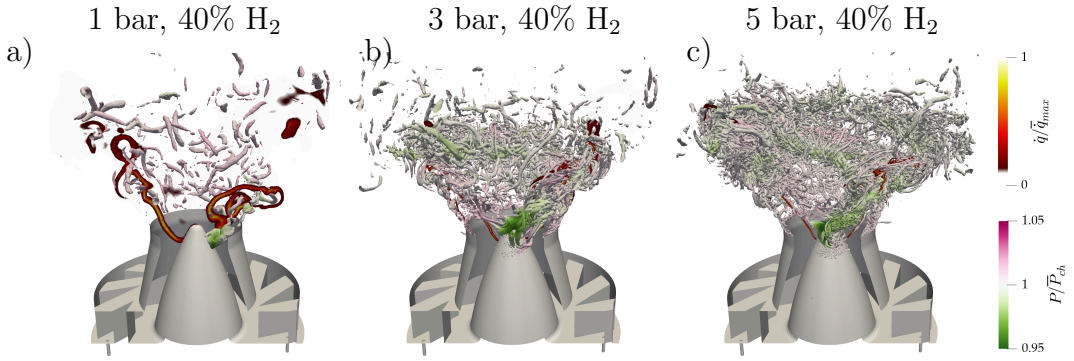

Figure 16: Comparison of instantaneous isocontour of Q-criterion at Q = 280 $\overline{U_x^2}/D_{inj}^2$ colored by pressure and field of normalized heat release rate $\dot{q}$ for Cases (a) *P1H40*, (b) *P3H40* and (c) *P5H40*.

5.3. Turbulent reactive flow time scales

Increasing pressure modifies the Reynolds number, affecting the flow turbulence scales (Table 2). This effect is clearly visible in Fig. 16, which compares instantaneous isocontour of Q-criterion at Q = 280 $\overline{U_x^2}/D_{inj}^2$ colored by pressure and fields of normalized heat release rate $\dot{q}$ for (a) Case *P1H40*, (b) Case *P3H40* and (c) Case *P5H40*. While the PVC is clearly present in all cases as also observed experimentally by Chterev and Boxx [45], the dimensions and the structures of the vortical structures change. In this case, according to the increase in Reynolds number, when pressure increases, vortices become smaller and more numerous, potentially changing the interaction with the flame front due to the reduction in the turbulent time and length scales.

Pressure also affects chemical reactions. Figure 17 presents instantaneous fields of measured OH-PLIF signal (top), computed OH mass fraction Y_{OH} (middle), heat release rate $\dot{q}$ (left, bottom) and flow vorticity normal to the plane $\omega_\perp$ (right, bottom) for (a) Case *P1H40*, (b) Case *P3H40* and (c) Case

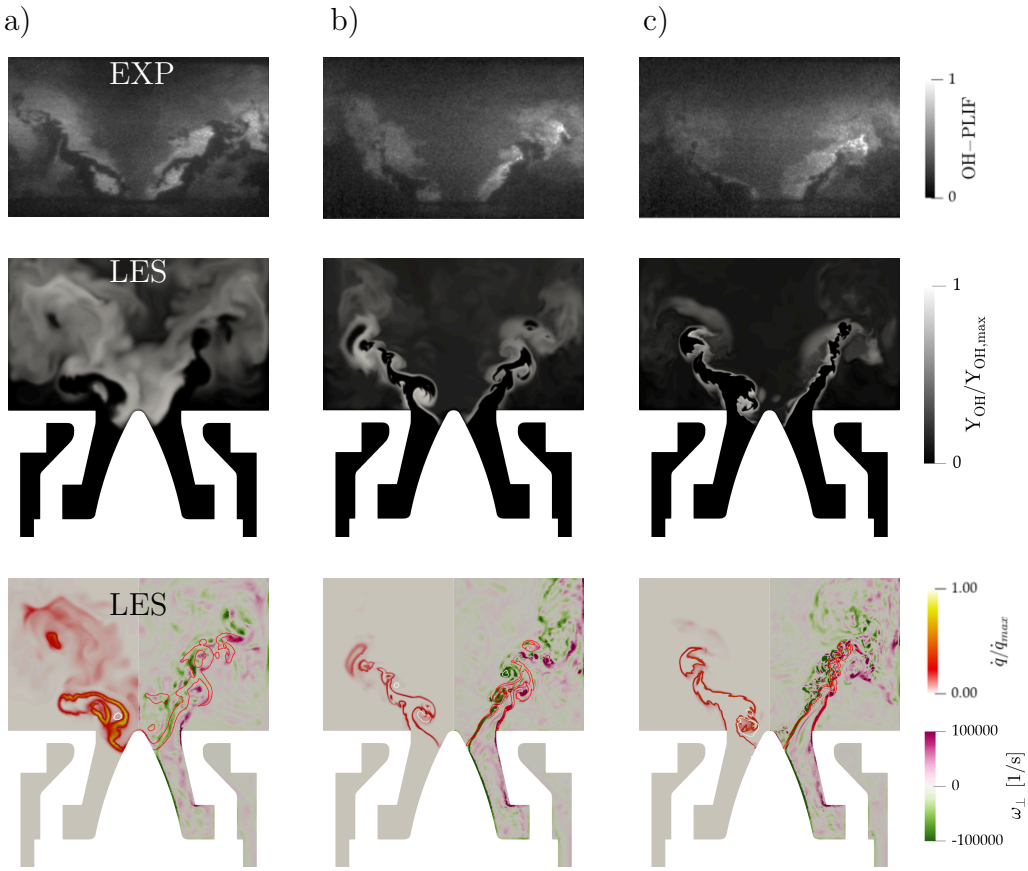

Figure 17: Instantaneous fields of the experimentally measured OH-PLIF signal (top), LES-predicted OH mass fraction Y_{OH} (middle), heat release rate $\dot{q}$ (left, bottom) and flow vorticity normal to the plane $\omega_\perp$ (right, bottom). Red and white isocontour refer to heat release rate $\dot{q}$ at 10% of $\dot{q}_{max}$ and low pressure respectively. Cases (a) *P1H40*, (b) *P3H40* and (c) *P5H40*.

P5H40. Red and white isocontours represent heat release rate $\dot{q}$ at 10% of $\dot{q}_{max}$ and low pressure respectively. OH-PLIF images and computed OH fields clearly reveal the reduction in chemical time scale due to pressure. As pressure increases, the OH field gets thinner: since OH has a very long lifetime compared to that of the heat-release reactions persists in the burned gases long after the heat-release reactions are complete, further underlining

the strong reduction in chemical time scale τ_c. At the same time, computed heat release rate fields show that flame thickness is reduced at 3 and 5 bar: the flame front is significantly more corrugated by turbulence and vortical structures [4].

The Damköhler number is known to be a critical parameter affecting vortex/heat-release layer interaction [75]. Da has been reported to modify the interaction between the flame and the PVC. This has indeed two main effects on the flame: it leads to roll-up of the reaction zone at the flame base, increasing heat release rate and it can introduce considerable aerodynamic stretch yielding local quenching or extinction of the flame front [83]. A similar behavior is noted in Fig. 17. At low Damköhler number (a) at atmospheric pressure, the PVC clearly causes the flame to roll-up at the flame base with an increase of heat release rate and the propagation of the flame is affected by local quenching and extinction. Due to the high vortex-induced aerodynamic stretch, part of the heat release is delayed and shifted downstream. Eventually, flame pockets detach from the main flame branches and produce pockets of OH visible both in the experiments and LES. At higher Damköhler number (b-c) instead, when pressure is above 3 bar, the PVC causes the flame to roll-up and increases the local heat release rate. The vortex-induced aerodynamic stretch, however, appears to be lower and stretch does not seem to significantly affect reaction or the flame branches. Note that the proper prediction of such phenomena due to time scales change

[4]Note that in LES the correct prediction of flame thickness reduction is due to the mesh refinement procedure that allow to resolve the flame with the same thickening value, as illustrated in section 3

at elevated pressure needs adequate grid resolution criteria and hence it is possible thanks to careful attention devoted to the LES modeling.

6. Conclusions

The impacts of mean pressure and hydrogen addition on the stabilization and combustion dynamics of a partially-premixed swirled-stabilized flame were studied experimentally and numerically. Experimentally, the PRECCINSTA burner was operated at elevated pressure, up to 5 bar, and the natural gas flame was enriched up to 40% of H_2 by volume. Numerically, LES results were validated against experimentally measured quantities such as OH* chemiluminescence and OH-PLIF images, stereoscopic particle image velocimetry (sPIV) and pressure recordings data, providing satisfactory agreement for all quantities. Particular attention is devoted to the choice of the numerical modeling. An Analytically Reduced Chemistry (ARC) kinetic scheme is able to correctly describe the CH_4-H_2/Air chemistry at elevated pressure. Since pressure significantly impacts the turbulent reactive flow scales, Static Mesh Refinement (SMR) approach is used for discretizing the fluid domain and allow for correctly resolving the different flames with the same combustion modeling at all pressured. Four flames were hence selected for LES simulations. Case *P1H0* corresponds to the reference natural gas flame (1 bar, 0% H_2), while cases *P1H40*, *P3H40* and *P5H40* refer to 40% H_2-enriched flames at 1, 3 and 5 bar, respectively.

Hydrogen enrichment at atmospheric pressure affects the flame stabilization, its shape and the corresponding thermoacoustic response. Flame *P1H0* (1 bar, 0% H_2) presents a lifted M-shape with a strong Precessing Vortex Core

(PVC) and no significant thermoacoustic response. When hydrogen addition is considered (Case *P1H40*), the flame takes on an attached V-shape, the PVC is weaker and the flame couples with the combustion chamber first acoustic mode at 420 Hz in a limit-cycle thermoacoustic oscillation that is predicted by LES in satisfactory agreement with experimental data. Computation of the acoustic modes of the system through an Helmholtz solver show no significant differences, confirming that the different thermoacoustic response is due to the flame shape change. The latter is likely due to the notably higher flame speed and increased resistance to strain-induced extinction of the H_2-enriched flame.

Elevated pressure modifies in turn the flame shape, its thermoacoustic response and also the characteristic time scales of turbulent reactive flows. As pressure increases, Cases *P3H40* and *P5H40* yield attached M-shape flames that get shorter and more compact. The combustor becomes more noisy but the coupling between the first acoustic mode and the heat release rate, which was present at atmospheric conditions, disappears. No significant change in the first acoustic chamber mode is predicted by the Helmholtz solver, suggesting that the flame shape change is the critical parameter that explains the different thermoacoustic response at elevated pressure. Finally, pressure modifies the characteristic time scales of the turbulent reactive flow. As pressure raises, the Reynolds number increases, reducing the Kolmogorov turbulent scale and the turbulent time scale τ_k, hence changing the dimensions and the relative strength of the vortical structures. At the same time, the laminar flame speed, the thermal flame thickness and the chemical time scale τ_c decrease. While the decrease in turbulent and chemical time scales

are of the same order of magnitude (the Karlovitz number remains almost constant), the Damköhler number significantly increases with pressure, leading to a modification in the flame/vortical structures interaction.

Therefore, both hydrogen enrichment and elevated pressure are found to significantly affect the flame shape, its stabilization and the corresponding thermoacoustic response in the HIPOT PRECCINSTA burner. Change of flame shape is the key element of the different thermoacoutic response and it is likely due to the different flame properties linked to hydrogen enrichment and to the modification of the chemical and turbulent time scales linked to elevated pressure. For all cases, LES successfully predicts the complex turbulent reactive flow, hence confirming the potential of numerical simulations in investigating high-power density flames close to real engines operating conditions.

Acknowledgements and Fundings

This project has received funding from the H2020-MSC-ITN Grant Agreement No 766264 (MAGISTER), the MSCA Grant Agreement No 843958 (CLEANERFLAMES - D. Laera Individual Fellowship), the H2020 Grant Agreement 952181 (COEC - Center of Excellence in Combustion), the ERC H2020 Grant Agreement 682383 (HyBurn) and the ERC H2020 Grant Agreement 832248 (SCIROCCO). HPC resources from the PRACE Projects 2020225434 (FANTASTIC-H2) are also acknowledged.

References

[1] P. Wolf, G. Staffelbach, A. Roux, L. Gicquel, T. Poinsot, V. Moureau, Massively parallel les of azimuthal thermo-acoustic instabilities in annular gas turbines, Comptes Rendus Mécanique 337 (2009) 385–394.

[2] E. Lo Schiavo, D. Laera, E. Riber, L. Gicquel, T. Poinsot, Effects of liquid fuel/wall interaction on thermoacoustic instabilities in swirling spray flames, Combust. Flame 219 (2020) 86–101.

[3] Y. Sommerer, D. Galley, T. Poinsot, S. Ducruix, F. Lacas, D. Veynante, Large eddy simulation and experimental study of flashback and blow-off in a lean partially premixed swirled burner, J. Turbul. 5 (37) (2004) 1–3.

[4] L. Esclapez, P. C. Ma, E. Mayhew, R. Xu, S. Stouffer, T. Lee, H. Wang, M. Ihme, Fuel effects on lean blow-out in a realistic gas turbine combustor, Combust. Flame 181 (2017) 82–99.

[5] F. Rebosio, A. Widenhorn, B. Noll, M. Aigner, Numerical simulation of a gas turbine model combustor operated near the lean extinction limit, in: ASME Turbo Expo 2010, Paper No. GT2010-22751, pp. 603–612.

[6] L. Y. Gicquel, G. Staffelbach, T. Poinsot, Large eddy simulations of gaseous flames in gas turbine combustion chambers, Prog. Energ. Combust. 38 (2012) 782–817.

[7] P. W. Agostinelli, Y. H. Kwah, S. Richard, G. Exilard, J. R. Dawson, L. Gicquel, T. Poinsot, Numerical and experimental flame stabilization analysis in the new spinning combustion technology framework, in:

ASME Turbo Expo 2020, Paper No. GT2020-15035, p. V04AT04A058 (13 pages).

[8] T. Poinsot, Prediction and control of combustion instabilities in real engines, Proc. Combust. Inst. 36 (2017) 1–28.

[9] U. Stopper, M. Aigner, H. Ax, W. Meier, R. Sadanandan, M. Stöhr, A. Bonaldo, Piv, 2d-lif and 1d-raman measurements of flow field, composition and temperature in premixed gas turbine flames, Exp. Therm Fluid Sci. 34 (2010) 396–403.

[10] C. D. Slabaugh, A. C. Pratt, R. P. Lucht, S. E. Meyer, M. Benjamin, K. Lyle, M. Kelsey, The development of an optically accessible, high-power combustion test rig, Rev. Sci. Instrum. 85 (2014) 035105.

[11] I. Boxx, C. Slabaugh, P. Kutne, R. P. Lucht, W. Meier, 3 kHz PIV/OH-PLIF measurements in a gas turbine combustor at elevated pressure, Proc. Combust. Inst. 35 (2015) 3793–3802.

[12] K. Peter Geigle, R. Hadef, W. Meier, Soot formation and flame characterization of an aero-engine model combustor burning ethylene at elevated pressure, J. Eng. Gas Turbines Power 136 (2014) 021505.

[13] C. D. Slabaugh, A. C. Pratt, R. P. Lucht, Simultaneous 5 kHz OH-PLIF/PIV for the study of turbulent combustion at engine conditions, Appl. Phys. B 118 (2015) 109–130.

[14] S. Dhanuka, J. Driscoll, H. Mongia, Instantaneous flow structures in a reacting gas turbine combustor, in: 44th AIAA/ASME/SAE/ASEE Joint Propulsion Conference & Exhibit, 2008, p. 4683.

[15] P. Malbois, E. Salaun, F. Frindt, G. Cabot, B. Renou, F. Grisch, L. Bouheraoua, H. Verdier, S. Richard, Experimental investigation with optical diagnostics of a lean-premixed aero-engine injection system under relevant operating conditions, in: ASME Turbo Expo 2017, Paper No. GT2017-64484, p. V04BT04A022.

[16] I. Chterev, N. Rock, H. Ek, B. Emerson, J. Seitzman, N. Jiang, S. Roy, T. Lee, J. Gord, T. Lieuwen, Simultaneous imaging of fuel, OH, and three component velocity fields in high pressure, liquid fueled, swirl stabilized flames at 5kHz, Combust. Flame 186 (2017) 150–165.

[17] J. Zhang, A. Ratner, Effect of pressure variation on acoustically perturbed swirling flames, Proc. Combust. Inst. 36 (2017) 3881–3888.

[18] B. Schuermans, F. Guethe, D. Pennell, D. Guyot, C. O. Paschereit, Thermoacoustic modeling of a gas turbine using transfer functions measured under full engine pressure, J. Eng. Gas Turbines Power 132 (2010) 111503.

[19] F. Di Sabatino, T. F. Guiberti, W. R. Boyette, W. L. Roberts, J. P. Moeck, D. A. Lacoste, Effect of pressure on the transfer functions of premixed methane and propane swirl flames, Combust. Flame 193 (2018) 272–282.

[20] Y. Xia, D. Laera, W. P. Jones, A. S. Morgans, Numerical prediction of the flame describing function and thermoacoustic limit cycle for a pressurised gas turbine combustor, Combust. Sci. Technol. 191 (2019) 979–1002.

[21] C. D. Slabaugh, I. Boxx, S. Werner, R. P. Lucht, W. Meier, Structure and dynamics of premixed swirl flames at elevated power density, AIAA J. 54 (2016) 946–961.

[22] R. Zhang, I. Boxx, W. Meier, C. D. Slabaugh, Coupled interactions of a helical precessing vortex core and the central recirculation bubble in a swirl flame at elevated power density, Combust. Flame 202 (2019) 119–131.

[23] P. Moin, S. V. Apte, Large-eddy simulation of realistic gas turbine combustors, AIAA J. 44 (2006) 698–708.

[24] G. Boudier, L. Gicquel, T. Poinsot, D. Bissières, C. Bérat, Comparison of les, rans and experiments in an aeronautical gas turbine combustion chamber, Proc. Combust. Inst. 31 (2007) 3075–3082.

[25] G. Boudier, L. Gicquel, T. Poinsot, Effects of mesh resolution on large eddy simulation of reacting flows in complex geometry combustors, Combust. Flame 155 (2008) 196–214.

[26] P. Schmitt, T. Poinsot, B. Schuermans, K. P. Geigle, Large-eddy simulation and experimental study of heat transfer, nitric oxide emissions and combustion instability in a swirled turbulent high-pressure burner, J. Fluid Mech. 570 (2007) 17–46.

[27] T. Jaravel, E. Riber, B. Cuenot, G. Bulat, Large Eddy Simulation of an industrial gas turbine combustor using reduced chemistry with accurate pollutant prediction, Proc. Combust. Inst. 36 (2017) 3817–3825.

[28] S. Legros, C. Brunet, P. Domingo-Alvarez, P. Malbois, E. Salaun, G. Godard, M. Caceres, B. Barviau, G. Cabot, B. Renou, G. Lartigue, V. Moureau, S. Puggelli, S. Richard, M. A. Boukhalfa, F. Grisch, Combustion for aircraft propulsion: Progress in advanced laser-based diagnostics on high-pressure kerosene/air flames produced with low-NOx fuel injection systems, Combust. Flame 224 (2021) 273–294.

[29] G. Oztarlik, L. Selle, T. Poinsot, T. Schuller, Suppression of instabilities of swirled premixed flames with minimal secondary hydrogen injection, Combust. Flame 214 (2020) 266–276.

[30] H. Yilmaz, O. Cam, I. Yilmaz, Experimental investigation of flame instability in a premixed combustor, Fuel 262 (2020) 116594.

[31] G. Zang, J. Zhang, J. Jia, E. S. Lora, A. Ratner, Life cycle assessment of power-generation systems based on biomass integrated gasification combined cycles, Renew. Energy 149 (2020) 336–346.

[32] P. S. P. Corrêa, J. Zhang, E. E. S. Lora, R. V. Andrade, L. R. de Mello e Pinto, A. Ratner, Experimental study on applying biomass-derived syngas in a microturbine, Appl. Therm. Eng. 146 (2019) 328–337.

[33] V. Di Sarli, A. D. Benedetto, Laminar burning velocity of hydrogen–methane/air premixed flames, Int. J. Hydrog. Energy 32 (2007) 637–646.

[34] Z. Chen, Effects of hydrogen addition on the propagation of spherical methane/air flames: A computational study, Int. J. Hydrog. Energy 34 (2009) 6558–6567.

[35] T. Boushaki, Y. Dhué, L. Selle, B. Ferret, T. Poinsot, Effects of hydrogen and steam addition on laminar burning velocity of methane-air premixed flame: Experimental and numerical analysis, Int. J. Hydrog. Energy 37 (2012) 9412–9422.

[36] C. Jiménez, D. Michaels, A. F. Ghoniem, Stabilization of ultra-lean hydrogen enriched inverted flames behind a bluff–body and the phenomenon of anomalous blow–off, Combust. Flame 191 (2018) 86–98.

[37] Y. J. Kim, B. J. Lee, H. G. Im, Hydrodynamic and chemical scaling for blow-off dynamics of lean premixed flames stabilized on a meso-scale bluff-body, Proc. Combust. Inst. 37 (2019) 1831–1841.

[38] T. Guiberti, D. Durox, P. Scouflaire, T. Schuller, Impact of heat loss and hydrogen enrichment on the shape of confined swirling flames, Proc. Combust. Inst. 35 (2015) 1385–1392.

[39] S. Shanbhogue, Y. Sanusi, S. Taamallah, M. Habib, E. Mokheimer, A. Ghoniem, Flame macrostructures, combustion instability and extinction strain scaling in swirl-stabilized premixed CH4/H2 combustion, Combust. Flame 163 (2016) 494–507.

[40] R. K. Cheng, D. Littlejohn, P. A. Strakey, T. Sidwell, Laboratory investigations of a low-swirl injector with H2 and CH4 at gas turbine conditions, Proc. Combust. Inst. 32 (2009) 3001–3009.

[41] B. Ge, Y. Ji, Z. Zhang, S. Zang, Y. Tian, H. Yu, M. Chen, G. Jiao, D. Zhang, Experiment study on the combustion performance of

hydrogen-enriched natural gas in a DLE burner, Int. J. Hydrog. Energy 44 (2019) 14023–14031.

[42] J. Zhang, A. Ratner, Experimental study on the excitation of thermoacoustic instability of hydrogen-methane/air premixed flames under atmospheric and elevated pressure conditions, Int. J. Hydrog. Energy 44 (2019) 21324–21335.

[43] P. Palies, M. Ilak, R. Cheng, Transient and limit cycle combustion dynamics analysis of turbulent premixed swirling flames, J. Fluid Mech. 830 (2017) 681–707.

[44] X. Kang, R. J. Gollan, P. A. Jacobs, A. Veeraragavan, Suppression of instabilities in a premixed methane–air flame in a narrow channel via hydrogen/carbon monoxide addition, Combust. Flame 173 (2016) 266–275.

[45] I. Chterev, I. Boxx, Effect of hydrogen enrichment on the dynamics of a lean technically premixed elevated pressure flame, Combust. Flame 225 (2021) 149–159.

[46] K. Oberleithner, S. Terhaar, L. Rukes, C. O. Paschereit, Why nonuniform density suppresses the precessing vortex core, J. Eng. Gas Turbines Power 135 (2013) 121506.

[47] K. Oberleithner, M. Stöhr, S. H. Im, C. M. Arndt, A. M. Steinberg, Formation and flame-induced suppression of the precessing vortex core in a swirl combustor: Experiments and linear stability analysis, Combust. Flame 162 (2015) 3100–3114.

[48] J. Beita, M. Talibi, S. Sadasivuni, R. Balachandran, Thermoacoustic instability considerations for high hydrogen combustion in lean premixed gas turbine combustors: A review, Hydrogen 2 (2021) 33–57.

[49] E. Æsøy, J. G. Aguilar, S. Wiseman, M. R. Bothien, N. A. Worth, J. R. Dawson, Scaling and prediction of transfer functions in lean premixed h2/ch4-flames, Combust. Flame 215 (2020) 269–282.

[50] Z. Lim, J. Li, A. S. Morgans, The effect of hydrogen enrichment on the forced response of ch4/h2/air laminar flames, Int. J. Hydrog. Energy 46 (2021) 23943–23953.

[51] J. Yoon, S. Joo, J. Kim, M. C. Lee, J. G. Lee, Y. Yoon, Effects of convection time on the high harmonic combustion instability in a partially premixed combustor, Proc. Combust. Inst. 36 (2017) 3753–3761.

[52] J. Peng, Z. Cao, X. Yu, S. Yang, Y. Yu, H. Ren, Y. Ma, S. Zhang, S. Chen, Y. Zhao, Analysis of combustion instability of hydrogen fueled scramjet combustor on high-speed OH-PLIF measurements and dynamic mode decomposition, Int. J. Hydrog. Energy 45 (2020) 13108–13118.

[53] N. A. Baraiya, S. R. Chakravarthy, Effect of syngas composition on high frequency combustion instability in a non-premixed turbulent combustor, Int. J. Hydrog. Energy 44 (2019) 6299–6312.

[54] J. Zhang, A. Ratner, Experimental study of the effects of hydrogen addition on the thermoacoustic instability in a variable-length combustor, Int. J. Hydrog. Energy 46 (2021) 16086–16100.

[55] S. Nakaya, K. Omi, T. Okamoto, Y. Ikeda, C. Zhao, M. Tsue, H. Taguchi, Instability and mode transition analysis of a hydrogen-rich combustion in a model afterburner, Proc. Combust. Inst. 38 (2021) 5933–5942.

[56] A. Datta, S. Gupta, S. Hemchandra, I. Chterev, I. Boxx, Impact of Hydrogen Addition on the Thermoacoustic Instability and processing vortex core dynamics in CH_4/H_2/Air technically premixed combustor, J. Eng. Gas Turb. Power 144 (2022) 021013.

[57] A. Kushwaha, P. Kasthuri, S. A. Pawar, R. I. Sujith, I. Chterev, I. Boxx, Dynamical Characterization of Thermoacoustic Oscillations in a Hydrogen-Enriched Partially Premixed Swirl-Stabilized Methane/Air Combustor, J. Eng. Gas Turb. Power 143 (2022) 121022.

[58] T. Indlekofer, B. Ahn, Y. H. Kwah, S. Wiseman, M. Mazur, J. R. Dawson, N. A. Worth, The effect of hydrogen addition on the amplitude and harmonic response of azimuthal instabilities in a pressurized annular combustor, Combust. Flame 228 (2021) 375–387.

[59] B. Ahn, T. Indlekofer, J. Dawson, N. Worth, Transient thermoacoustic responses of methane/hydrogen flames in a pressurized annular combustor, J. Eng. Gas Turb. Power 144 (2022) 011018.

[60] B. Higgins, M. Q. McQuay, F. Lacas, J. C. Rolon, N. Darabiha, S. Candel, Systematic measurements of OH chemiluminescence for fuel-lean, high-pressure, premixed, laminar flames, Fuel 80 (2001) 67–74.

[61] O. Colin, M. Rudgyard, Development of High-Order Taylor-Galerkin Schemes for LES, J. Comput. Phys. 162 (2000) 338–371.

[62] F. Nicoud, H. B. Toda, O. Cabrit, S. Bose, J. Lee, Using singular values to build a subgrid-scale model for large eddy simulations, Phys. Fluids 23 (2011) 085106.

[63] J. P. Legier, T. Poinsot, D. Veynante, Dynamically thickened flame LES model for premixed and non-premixed turbulent combustion, Proc. Summer Program, Cent. Turbul. Res. (2000) 157–168.

[64] F. Charlette, D. Veynante, C. Meneveau, A power-law wrinkling model for LES of premixed turbulent combustion: Part I - non-dynamic formulation and initial tests, Combust. Flame 131 (2002) 159–180.

[65] P. S. Volpiani, T. Schmitt, D. Veynante, Large eddy simulation of a turbulent swirling premixed flame coupling the TFLES model with a dynamic wrinkling formulation, Combust. Flame 180 (2017) 124–135.

[66] E. Ranzi, A. Frassoldati, A. Stagni, M. Pelucchi, A. Cuoci, T. Faravelli, Reduced kinetic schemes of complex reaction systems: Fossil and biomass-derived transportation fuels, Int. J. Chem. Kinet. 46 (2014) 512–542.

[67] Q. Cazères, P. Pepiot, E. Riber, B. Cuenot, A fully automatic procedure for the analytical reduction of chemical kinetics mechanisms for computational fluid dynamics applications, Fuel 303 (2021) 121247.

[68] D. Laera, P. W. Agostinelli, L. Selle, Q. Cazères, G. Oztarlik, T. Schuller, L. Gicquel, T. Poinsot, Stabilization mechanisms of CH4

premixed swirled flame enriched with a non-premixed hydrogen injection, Proc. Combust. Inst. 38 (2021) 6355–6363.

[69] T. Poinsot, S. Lele, Boundary conditions for direct simulations of compressible viscous flows, J. Comput. Phys. 101 (1992) 104–129.

[70] P. W. Agostinelli, D. Laera, I. Boxx, L. Gicquel, T. Poinsot, Impact of wall heat transfer in Large Eddy Simulation of flame dynamics in a swirled combustion chamber, Combust. Flame 234 (2021) 111728.

[71] M. F. Modest, Radiative heat transfer, Academic press, 2013.

[72] W. L. Grosshandler, RADCAL: A Narrow Band Model for Radiation, NIST Tech. note 1402, 1993.

[73] S. B. Pope, Turbulent flows, IOP Publishing, 2001.

[74] T. Poinsot, D. Veynante, Theoretical and numerical combustion, RT Edwards, Inc., 2005.

[75] K. Ahn, K. H. Yu, Effects of Damköhler number on vortex-flame interaction, Combust. Flame 159 (2012) 686–696.

[76] P. W. Agostinelli, B. Rochette, D. Laera, J. Dombard, B. Cuenot, L. Gicquel, Static mesh adaptation for reliable large eddy simulation of turbulent reacting flows, Phys. Fluids 33 (2021) 035141.

[77] R. Schefer, D. Wicksall, A. Agrawal, Combustion of hydrogen-enriched methane in a lean premixed swirl-stabilized burner, Proc. Combust. Inst. 29 (2002) 843–851.

[78] J.-Y. Ren, W. Qin, F. Egolfopoulos, T. Tsotsis, Strain-rate effects on hydrogen-enhanced lean premixed combustion, Combust. Flame 124 (2001) 717–720.

[79] J. Hunt, A. Wray, P. Moin, Eddies, stream, and convergence zones in turbulent ows., in: Annual Research Briefs, Center for Turbulence Research, Center for Turbulence Research, NASA Ames/Stanford Univ., 1988, pp. 193–208.

[80] F. Nicoud, L. Benoit, C. Sensiau, T. Poinsot, Acoustic modes in combustors with complex impedances and multidimensional active flames, AIAA J. 45 (2007) 426–441.

[81] W. Meier, P. Weigand, X. Duan, R. Giezendanner-Thoben, Detailed characterization of the dynamics of thermoacoustic pulsations in a lean premixed swirl flame, Combust. Flame 150 (2007) 2–26.

[82] D. Durox, T. Schuller, N. Noiray, S. Candel, Experimental analysis of nonlinear flame transfer functions for different flame geometries, Proc. Combust. Inst. 32 I (2009) 1391–1398.

[83] M. Stöhr, C. M. Arndt, W. Meier, Effects of Damköhler number on vortex-flame interaction in a gas turbine model combustor, Proc. Combust. Inst. 34 (2013) 3107–3115.